COLORADO
Department of Transportation

CDOT Applied Research and Innovation Branch

Snow Depth Retrieval with an Autonomous UAV-Mounted Software-Defined Radar

Samuel Prager, Graham Sexstone, Daniel McGrath, John Fulton, Mahta Moghaddam

April 2023

CDOT-2023-03

Technical Report Documentation Page

1. Report No.	2. Government Accession No.	3. Recipient's Catalog No.
CDOT-2023-03		

4. Title and Subtitle	5. Report Date
Snow Depth Retrieval with an Autonomous UAV-Mounted Software-Defined Radar	April 2023
	6. Performing Organization Code

7. Author(s)	8. Performing Organization Report No.
Samuel Prager, Graham Sexstone, Daniel McGrath, John Fulton, Mahta Moghaddam	

9. Performing Organization Name and Address	10. Work Unit No. (TRAIS)
Colorado Water Science Center U.S. Geological Survey Box 25046, Mail Stop 415 Denver, CO 80225	11. Contract or Grant No. R219.03 - UASnow - USGS

12. Sponsoring Agency Name and Address	13. Type of Report and Period Covered
Colorado Department of Transportation Applied Research and Innovation Branch 2829 W. Howard Place Denver, CO 80204	Final
	14. Sponsoring Agency Code

15. Supplementary Notes

Prepared in cooperation with the US Department of Transportation, Federal Highway Administration

16. Abstract

We present results from a field campaign to measure seasonal snow depth at Cameron Pass, Colorado, using a synthetic ultrawideband software-defined radar (SDRadar) implemented in commercially available Universal Software Radio Peripheral (USRP) software-defined radio hardware and flown on a small hexacopter unmanned aerial vehicle (UAV). We coherently synthesize an ultrawideband signal from stepped frequency 50-MHz subpulses across 600-2100-MHz frequency bands using a novel nonuniform nonlinear synthetic wideband waveform reconstruction technique that minimizes sweep time and completely eliminates problematic grating lobes and other processing artifacts traditionally seen in stepped waveform synthesis. We image seasonal snow across two transects: a 400-m open Meadow Transect and a 380-m forested transect. We present a surface detection algorithm that fuses data from LiDAR, global navigation satellite system (GNSS)/global positioning system (GPS), and features in the radargram itself to obtain high precision estimates of both snow and ground surface reflections, and thus total snow depth, represented as two-way travel time. The measurements are validated against independent ground-based ground-penetrating radar measurements with correlations coefficients as high as • = 0.9 demonstrated. Finally, we compare backscattered radar data collected by the UAV-SDRadar while hovering proximal to a known snow pit with in situ measured snow dielectric profiles and demonstrate imaging of snow stratigraphy.

17. Keywords	18. Distribution Statement
Snow depth, software-defined radar (SDRadar), stratigraphy, synthetic wideband waveform (SWW), unmanned aerial vehicle (UAV).	This document is available on CDOT's website: https://www.codot.gov/programs/research

19. Security Classif. (of this report)	20. Security Classif. (of this page)	21. No. of Pages	22. Price
Unclassified	Unclassified	33 pages	

Table of Contents

List of Figures

List of Tables

Acknowledgments

The authors should recognize the USGS Innovation Center, USGS Hydrogeophysics Branch, USGS National UAS Project Office, and Drone Amplified. They thank Randall Bonnell and Alex Olsen-Mikitowicz for assistance in the field. Because of the proprietary nature of the UAV-SDRadar and the code used to process the radargrams, data either are not avail-able or have limited availability. Please contact S. Prager (sprager@usc.edu) at the University of Southern California for more information.

Personnel from the Colorado State University collected the ground-truth data used to validate the performance of the UAV-SDRadar and did not receive funding to collect or process the data either from the University of Southern California or the U.S. Geological Survey. Any use of trade, firm, or product names is for descriptive purposes only and does not imply endorsement by the U.S. Government.

Executive Summary

The contents of this report were also published in 2020 in IEEE Transactions on Geoscience and Remote Sensing, volume 6. It discusses a method for measuring snow depth and snow layers using an Unmanned Aerial Vehicle (UAV) equipped with a synthetic ultrawideband software-defined radar (SDR) implemented in commercially available Universal Software Radio Peripheral (USRP) software-defined radio hardware. The research focuses on the efficacy of this autonomous system to efficiently measure snow thickness and layering in various environments. By leveraging standard ground-based snow measurements, the accuracy of the radar can be improved and be adapted to operations in different environmental conditions, improving the accuracy, and reliability of non-contact snow measurements. This approach has potential applications in environmental monitoring, climate research, and resource management.

The findings demonstrated the successful use of a novel Synthetic Wideband Waveform Non-Uniform Frequency Stitching (SWW NUFS) algorithm in an ultrawideband SDRadar sensor on a UAV platform to measure distributed snow depth at a field site in Colorado. Using a low-cost Commercial-off-the-Shelf (COTS) USRP SDR-based SDRadar sensor, we have demonstrated tunable coherent ultrawideband radar operation from a moving UAV platform with complete removal of grating lobes and other signal processing artifacts. This is the first successful demonstration of UAV-based radar imaging and retrieval of snow depth in a heavily forested area and the first integration of UAV-based radar, Structure from Motion-Multi-View Stereo (SfM-MVS), and Light Detection and Ranging (LiDAR) altimetry data for snowpack mapping. We have validated the UAV-SDRadar results with ground-based Ground Penetrating Radar (GPR) sled measurements, making this the first field campaign with results from UAV-based radar compared with GPR-derived ground truth.

We have also imaged snow layer stratigraphy from a UAV-SDRadar and compared the results with snow pit dielectric measurements. We have shown successful UAV platform motion compensation using RTK/PPK GNSS/GPS sensor and topography compensation using both independent SfM measurements and an original surface detection algorithm that incorporates LiDAR altimetry data and radargram features to identify snow and ground interfaces.

I. Introduction

Mapping of the water stored in snowpacks or snow water equivalent (SWE) at high resolution on a global surface and subsurface hydrologic processes [1]. Due to the high variability of snow distribution and dynamics across diverse landscapes, there is a critical need for the emergence of technologies that are not only capable of high spatial resolution but also deployable over large spatial extents and across varied and rugged terrain [2]. In mountainous environments of the western United States (U.S.), seasonal snowmelt runoff is a major source for streamflow and subsurface recharge across much of the region [3]. Therefore, quantifying and tracking the amount of water stored within seasonal snow are critically important for water resources forecasting and planning.

The seasonal snowpack is often highly variable over space and through time in mountainous regions [4] as a result of the driving influences of meteorology (e.g., precipitation, temperature, vapor pressure, wind, and net radiation) on the snowpack and its interactions with terrain and forest canopy features [5]. These complex processes controlling snow evolution at fine spatial scales make monitoring the spatial variability of the seasonal snowpack a substantial challenge.

There is great potential in using satellite and airborne remote sensing platforms for monitoring the spatiotemporal variability of the seasonal snowpack that cannot be done by traditional field measurements. However, there are still major challenges limiting the direct observation of snow distributions in mountainous and other environments, and at present, no single method provides distributed SWE on global scales at high spatial resolution [6]. Estimating SWE requires measurement of: 1) snow cover extent; 2) snow depth; and 3) snow density.

Background soil characteristics, submerged vegetation, forest cover, and steep terrain all pose challenges in remote sensing of snowpack characteristics (including SWE) on a global scale, and new snow measurement techniques are needed for improved snow observations as outlined in the National Aeronautics and Space Administration (NASA) SnowEx Science Plan [1]. Of these new measurement techniques, radar is listed as a promising technology for snowpack monitoring because of its ability to penetrate vegetation and forest cover at certain frequencies and the potential for direct SWE retrieval from volume scattering or SWE change detection using interfero-metric synthetic aperture radar (InSAR) phase differences [1]. Furthermore, there has been much recent excitement surrounding the potential of small multicopter aircraft as a viable path for widespread deployment of snow/ice imaging radar sensors although the capabilities of such systems are as of yet largely unquantified [7].

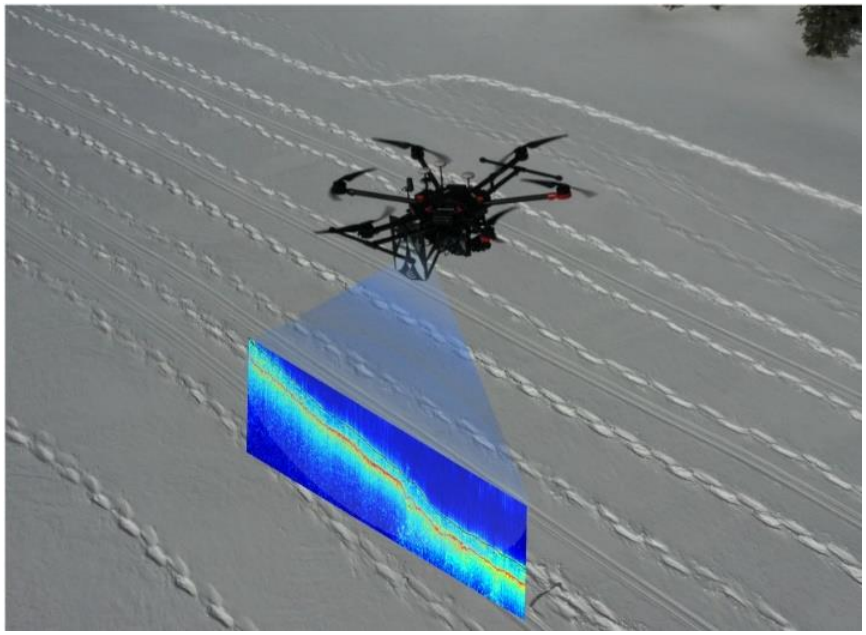

Figure 1. Illustration of sUAS-based UAV-SDRadar system performing syn-thetic ultrawideband radar measurements of snow depth while flying over snow covered meadow at Cameron Pass, Colorado.

In this work, we demonstrate snow depth retrieval across variable terrain with an autonomous multicopter small unmanned aircraft system (sUAS) consisting of a synthetic wideband waveform (SWW) software-defined radar (SDRadar) sensor implemented in a low-cost commercial off-the-shelf (COTS) software-defined radio (SDR), a DJI M600 hexacopter unmanned aerial vehicle (UAV), and ground control station. The UAV-mounted SDRadar (UAV-SDRadar) system is shown in flight over the study site in Fig. 1. We operate the UAV-SDRadar system, as shown on the ground in Fig. 2(a), over both meadow and forested transects and validate the results with measurements taken by a ground-based sled ground-penetrating radar (GPR) system, as seen in Fig. 2(b).

The objectives of this research are to: 1) demonstrate snow depth retrieval across varied terrain from an sUAS-based radar system validated with ground-based GPR measurements; 2) develop radar processing and surface detection algorithms specifications to sUAS-based radar platforms to further enable autonomous operation and measurement; 3) demonstrate the use of widely available open-source COTS SDR hardware for high-resolution radar applications from sUAS platforms using synthetic wideband techniques; and 4) quantify the performance of sUAS-based radar system in varied terrain including both open and forested regions, the latter of which is identified as the first of seven critical gaps in current remote sensing technologies in the NASA SnowEx Science Plan [1]. This report was originally published in its entirety by IEEE Transactions on Geoscience and Remote Sensing, 60, p. 1-16,

https://ieeexplore.ieee.org/document/9579463, https://doi: 10.1109/TGRS.2021.3117509. This report was reformatted to meet CDOT and FHWA reporting requirements

A list of acronyms used in this work can be found in Appendix A.

II. Background On Snow Observation Using Radar Systems

In the context of radar sensors, the most direct measurement is the two-way travel time (TWT) of the radar signal as it propagates through a medium and is reflected back to the receiver; at that point, the magnitude and phase of the scattered signal are measured.

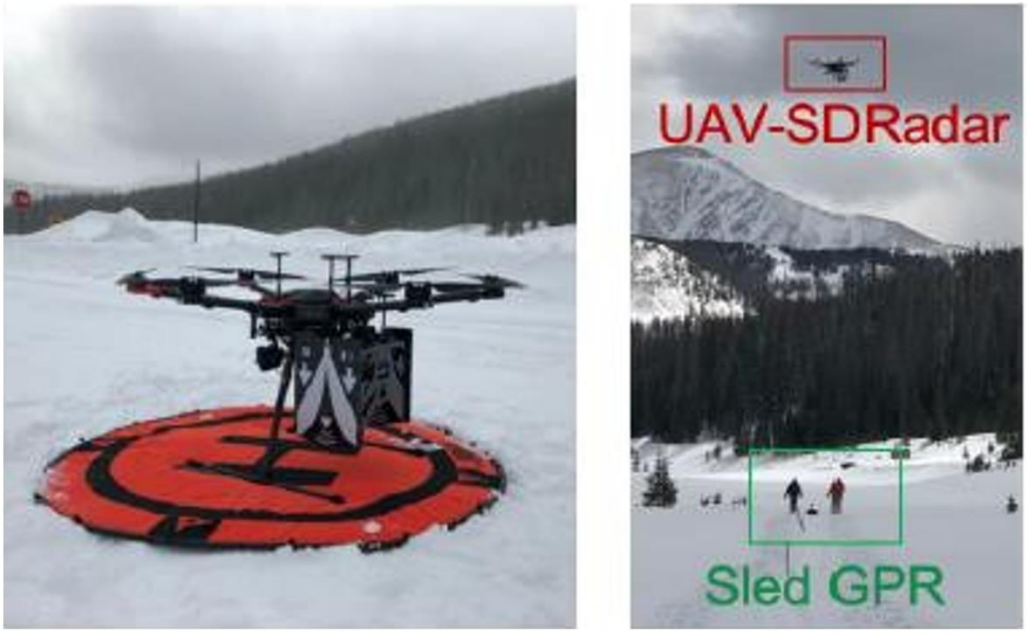

(a) (b)

Figure 2. UAV-SDRadar system and sled GPR team operating at Cameron Pass, Colorado, test site. (a) UAV-SDRadar sUAS consisting of a battery-powered USRP E312 SDR and two Vivaldi TX/RX antennas mounted on a DJI M600 hexacopter UAV. (b) UAV-SDRadar sUAS in flight over the Meadow Transect. The snow depth along the transect was measured by the UAV-SDRadar system and a ground-based sled GPR operated by the team as shown. Note that the landing gear of the UAV retracts in flight

The snow depth d_s is related to the TWT of a radar signal through the snow as

$$d_s = \frac{TWT}{2} \cdot \frac{c}{\sqrt{\epsilon_s}} \tag{1}$$

where ϵ_s is the relative dielectric permittivity of the snow and $c = 3 \times 10^8$ m/s is the speed of light in a vacuum [8].

For the dry snow, the permittivity is a direct function of snow density, ρ_s (gcm^{-3}), and the known dielectric of pure ice (typically ~3.15) [8]–[10]. Values for dry snow dielectric permittivity range from 1.0 to 1.9 as ice volume fraction, an indication of snow density, changes from 0 to 0.5 [11]. SWE is defined for a snow layer of height d_s as [9].

$$SWE = \int_0^{d_s} \rho_s \, dz \quad [cm] \tag{2}$$

In order to capture the high spatial variability of snowpack characteristics on the order of ~10 cm, high radar resolution and, thus, large bandwidth (BW), on the order of ~1 GHz, are required [12], [13].

Radar sensors capable of achieving such high resolution, particularly at the lower frequencies required to effectively penetrate snow and ice media, as well as vegetation layers, are typically expensive, power-hungry, and heavy. This is a substantial challenge in the widespread deployment of high-performance radar sensors on sUAS platforms.

The first report of a GPR/snow penetrating radar with high enough BW to resolve snow stratigraphy and low enough weight and power consumption to be flown as a small UAV payload successfully flown in a campaign to image snowfields was in 2020 [14], [15]. The authors were able to conduct a single flight, but no in situ measurements were collected due to weather and site access [15]. They used a UWB radar sensor developed by the German company Ilmsens and flew 1 m above the snow surface. A limitation of the m-sequence wave-form used in the Ilmsens radar is its low unambiguous range of 5.75 m, which constrains the maximum UAV height because of the relatively small unambiguous target window [14], [15]. The instrument did not penetrate into the ice during the airborne test. During the in situ test, the instrument was able to penetrate 14.5 and 170 cm at the Arctic sea and Kattfjordeidet test sites, respectively [15]. Improvements to the system and results from an extensive measurement campaign in Svalbard, Norway, which was compared with in situ snow depth, were reported in a subsequent publication [16]. The study consisted of five sites composed of 100 x 100 m grids and two 100-m transects and report a spatial correlation of 0.97 with in situ measurements. In addition, the authors address the range ambiguity of the m-sequence radar and resulting limitations on UAV height by using a laser altimeter and defining an “ambiguity window” of 5.75 m that contains the totality of the target. However, because of antenna crosstalk, this approach requires the UAV to fly in designated altitude zones so that the ambiguous echoed signal does not wrap into the higher power crosstalk signal [16]. The constraint of UAV height to either a maximum distance of 5.75 m above the ground surface or within designated altitude zones both requires apriori knowledge of the approximate snow depth and is not feasible for highly varied or rough terrain, particularly in the presence of both sparse and dense foliage or forests where the laser altimeter is obscured and/or erroneous. When feasible, a lower flight altitude

yields substantial improvements in the signal-to-noise ratio (SNR), and the tradeoff of unambiguous range limitations for very high spatial sampling pulse repetition frequency (PRF) in the m-sequence radar is justified for suitable environments.

Recently, measurements of snow depth over Antarctic sea ice from a UAV platform have been compared with manual snow probe depths [17]. The authors used an array of Vivaldi antennas and a vector network analyzer to perform ultrawideband stepped frequency continuous wave (SFCW) measurements of snow depth from a UAV.

The Center for Remote Sensing of Ice Sheets (CReSIS) has developed numerous radar instruments for ice and snow sounding. Flexible ultrawideband frequency modulated continuous wave (FMCW) radars operating over selectable bands ranging from 14 MHz to 38 GHz developed by CReSIS have been demonstrated in vertical ice column profile imaging and in alpine snow depth measurement [7],

[18]–[20]. Whereas the majority of current CReSIS instruments operate from traditional airborne platforms, the next-generation CreSIS instruments will be targeted for small multicopters [7]. For example, a CReSIS radar sensor deployed on a fixed-wing UAS was used to sound polar ice sheets [21],the first successful report of this kind, and efforts to integrate the CReSIS UWB Snow Mini Radar onto a small UAS helicopter have been explored [7].

As of 2021, there has been no comparison of multicopter sUAS-based radar snow depth retrievals with ground-based GPR data reported in the literature and no demonstration of sUAS radar systems in forested or topographically complex areas.

The use of GPR has become widespread in cryospheric research as a means of replacing the laborious and intensive process of digging snow pits and collecting manual snow probe data [2]. Previous literature has proven that GPR surveys can provide accurate and efficient measurements of snow depth and high-resolution imagery of snow layer stratigraphy [10], [22]–[27].

As part of a validation effort for NASA's SnowEx Mission, a large-scale field campaign in Grand Mesa, Colorado, was conducted to measure snow depth with GPR [10]. There was good agreement between GPR snow depth estimates and manual snow depth measurements (correlation coefficient $\rho = 0.89$), thus providing further evidence for GPR as an efficient means of collecting effectively ground-truth snow depth data [2], [22], [24], [26]. In addition, ground-based GPR results were compared with airborne LiDAR from the NASA Airborne Snow Observatory (ASO) and stereophotogrammetry from DigitalGlobe WorldView-3 satellite imagery, with reported correlation coefficients of 0.9 and 0.7, respectively [10].

Space and airborne [1], [7], [18], [19], [28], [29], as well as tower and fixed-line [6], [30], [31] radar systems, particularly higher frequency FMCW radars, have been demonstrated in snow depth measurement, snow stratigraphy imaging, and SWE retrieval. Oftentimes, higher frequency FMCW radars are selected to more easily achieve broad BW (and, therefore, resolution) at the expense of penetration depth. SWE retrieval via inversion of a forward scattering model has been demonstrated for dual-polarized X- and Ku-band SnowSAR data with a correlation coefficient of 0.64 [29]. Snow depth measurements obtained by a 2-18-GHz FMCW radar flown on a fixed-wing aircraft flying at a 500-m altitude have been reported with a correlation of 0.88 with in situ measurements [31].

Although space-borne and high-altitude airborne remote sensing methods are capable of coverage over vast areas, the resulting data products do not have the sufficiently high spatial resolution to capture the finer scale variability and dynamics that are critical to achieving a complete picture of cryospheric processes [1], [12].

Multiangle optical imagery and LiDAR-based approaches to snow depth measurements from sUAS platforms have been widely reported [12], [32]-[34]. Because of their high operational frequency, optical and LiDAR sensors can achieve high resolution with very small payload size, making them ideal for deployment on sUAS. Structure from Motion-Multi-View Stereo (SfM-MVS) processing uses a multiangle sequence of 2-D images, as well as precise UAV platform knowledge and a series of ground control points (GCPs) to create high-resolution 3-D surface models of structures and survey area topography [32], [33].

The fundamental shortcoming of optical and visible spectrum approaches to snow depth measurement, however, is that such sensors only measure the snow/ground surface; thus, repeat observations are required to detect changes in surface elevation. Furthermore, they are highly sensitive to estimated snow densities in order to convert the measured snow depth to SWE. In addition, in areas with dense foliage or with thick forest canopies, optical signals cannot penetrate to the snow and ground surfaces below to obtain accurate measurements, making subcanopy snow depth retrievals a persistent challenge [12].

Table 1. Specifications for USRP E312 SDR Hardware Used to Implement SDRadar [35]

Parameter	Value
Sampling Rate, f_s	50 MHz
Analog Bandwidth, B_s	56 MHz
Tunable Center Frequency, f_c	70 MHz – 6 GHz
TX Gain Range	0–89.5 dB
RX Gain Range	0–76 dB
Size	133 x 68.2 x 31.8 mm
Weight	446 g
Price	$3199.00

III. Hardware System

The core hardware component of the SDRadar system used in this work is the Universal Software Radio Peripheral (USRP) E312 SDR from Ettus Research, a National Instruments (NI) company. The USRP E312 is a battery-powered 2 x 2 MIMO SDR module based on the Analog Devices AD9361 Radio Frequency Integrated Circuit (RFIC) front end and the Xilinx Zynq-7020 FPGA + ARM Processor System on Chip (SoC). Specifications for the USRP E312 are given in Table I. The sensor payload also includes an SF11/C LiDAR altimeter from Lightware Optoelectronics and a Reach M2 RTK global navigation satellite system (GNSS)/global positioning system (GPS) module from Emlid Ltd., both of which are connected to the USRP E312 via USB port.

The USRP E312 runs a modified version of the USRP Hardware Driver (UHD), which has been optimized for high-performance stepped frequency radar. The software modifications include changes to the AD9361 register map configuration to guarantee coherence across channels, simplification of the frequency tuning routine for faster local oscillator (LO) phase-locked loop (PLL) locking, and fast-switching routines between calibration and data channels. Using the loopback channel, we precompute a frequency-to-gain lookup table in order to flatten the transmit power and receiver gain across the wide stepped frequency band. In addition, within the RF Network on Chip (RFNoC) infrastructure, we add to the FPGA design an arbitrary waveform generator (AWG), as well as a coherent transmit (TX)/receive (RX) pulse timing controller and TX/RX command generator to reduce the workload of the embedded ARM processor [36].

We implement a server–client architecture, wherein an asynchronous TCP/IP server has written in C++ runs on the USRP E312 SDRadar [36]. Heterogeneous client devices can send commands and receive data over ethernet, WiFi, or XBee serial radio. The SDRadar server program is capable of queuing and executing complete mission plans autonomously. The SDRadar server is also responsible for streaming data from both internal (GPS and IMU) and external (RTK GNSS and LiDAR altimeter) sensors, which are stored as timestamped radar pulse metadata. Received complex I/Q radar pulse data are stored onboard in the SDRadar internal SD Card and an achieved data rate of 1.49 MB/s. In addition, the SDRadar can broadcast radar data to a UDP port allowing all subscribed clients to process and visualize the radar data in real time.

A DJI Manifold 2 single-board computer (SBC), based on the NVIDIA Jetson TX2 GPU, is also flown on the aircraft.

Table 2. Size and Weight of UAV-SDRadar Peripheral Sensors and Modules

Module	Size	Weight
DJI Manifold 2 Jetson TX2 SBC	91 x 61 x 35 mm	230 g
Emlid M2 RTK GNSS/GPS	56.4 x 45.3 x 14.6 mm	35 g
SF11/C lidar altimeter	30 x 56.5 x 50 mm	35 g
RFSpace TSA600 Antenna(s)	240 x 330 x 1.5 mm	227 g
RF Amp (Minicircuits ZX60-V82-S+)	19.1 x 18.8 x 11.7 mm	23 g

The onboard Manifold 2 SBC runs the SDRadar Client C++ software and receives and processes real-time radar data from the UDP stream to form SWW radargrams that are transmitted as an HDMI video stream over the DJI M600 RF Link to the ground station.

We operate the SDRadar in a pseudobistatic configuration with two tapered slot Vivaldi TSA600 antennas from RF-Space used for TX and RX. The antennas have an operational frequency of 600 MHz– 6 GHz and a nominal beamwidth of 45^{o}. Extensive antenna testing and pattern measurements were performed by the Antenna Test Lab Company [37].

The complete UAV-SDRadar payload is flown on a DJI Matrice M600 Pro hexacopter UAV. The M600 UAV is flown autonomously on predefined flight paths using control soft-ware from Drone Amplified. The UAV runs on six 22.2-V 4500-mAh DJI TB47S batteries, with an estimated UAV power consumption of 2 kW. The maximum payload capacity of the UAV is 6 kg. The UAV flight time is 32 min with no payload and 16 min with a 6-kg payload at sea level [38]. The altitude at the test site was

9600 ft (2600 m). At this altitude with the 1.25-kg radar payload, the UAV flight time was ~18 min. The radar payload runs off of the internal USRP E312 3.7-V 3200-mAh battery. The radar payload power consumption is 2–6 W, with the battery lasting 2–3 h in normal operation.

Details on the sizes/weights of the peripheral sensors and modules are provided in Table II, and the hardware diagram of the complete system used in this effort is shown in Fig. 3. The complete system is shown mounted to the underside of the UAV in Fig. 2(a). An optical camera is also flown for situational awareness while operating the aircraft.

The direct path signal or crosstalk between the TX and RX antennas is a key factor affecting the performance of the sUAS radars [16]. The low flight altitude makes range-gating the received signal infeasible for pulse compression waveforms having sufficient time-BW product, and therefore, the crosstalk signal must be received along with the scattered target signal without saturating the receiver, limiting the maximum TX power of the system. The level of isolation between the TX/RX antennas required will depend on the UAV height above the ground surface, the surface dielectric, and other factors affecting the return signal strength. The separation between the TX/RX antennas shown in Fig. 2(a) is 0.34 m yielding isolation of ~30 dB. The radar has a dynamic range of ~65 dB depending on the window used and corresponding sidelobe roll-off, allowing us to detect a signal with ~95-dB path loss. In the current configuration, a unit radar cross section (RCS) target is detectable at a maximum range of ~240m.

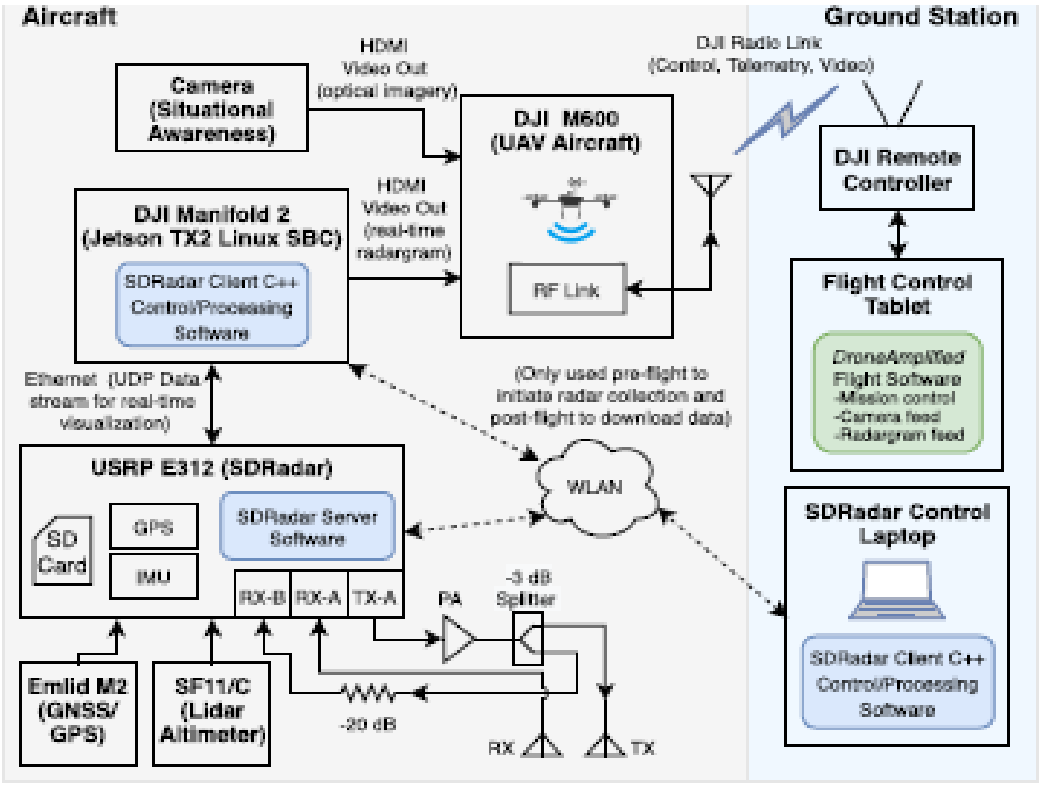

Figure 3. Diagram of sUAS system used for flight experiments. (Left) UAV-SDRadar system. (Right) Ground control system. Real-time telemetry and (optional) processed radargram live video feed is provided via high power DJI Radio Link. SDRadar configuration, mission control, and data download are done via WiFi Wireless Local Area Network (WLAN). The optional Jetson TX2 SBC (DJI Manifold 2) can process SWW radar data in real time and relay a live radargram video feed to the ground station. The radar data are also stored locally on the E312 SDRadar SD card for offline processing.

IV. SWW Reconstruction and Radar Processing

The radar signal processing consists of the following steps:

1) internal subpulse phase calibration;

2) subpulse system sky-calibration removal;

3) nonuniform frequency stitching (NUFS) to form the SWW (as described in Section IV-A);

4) 2-D SWW radargram construction;

5) rowwise complex mean subtraction across sweeps to remove direct path signal sidelobes and further reduce grating lobes;

6) range magnitude scaling and motion compensation to remove effects of UAV altitude variation;

7) columnwise moving average threshold filter;

8) columnwise mean power subtraction for each scan to reduce vertical striping;

9) columnwise moving median threshold filter to reduce speckle.

The complete radar signal processing is visualized in Fig. 4. We note that the horizontal lines present in the raw radargram at the bottom left of Fig. 4 are due to a combination of physical ringing between the TX and RX antennas, the sidelobes of the direct path signal, and minor residual processing artifacts due to the NUFS SWW reconstruction, as discussed further in Sections IV-A and IV-B.

A. SWW Reconstruction

In this section, we expand upon work previously reported in [39]. We now extend the frequency stacking (FS) SWW recon-struction technique [36]. It has been demonstrated that ultrawideband waveforms may be coherently synthesized from instantaneous BW- limited stepped-frequency subpulses to achieve centimeter-level resolution capability SDRadar using low- cost commercial SDR boards [36], [40]. An additional advantage of employing stepped-frequency techniques in SDRadar is that spectrum usage is easily managed by configuring the operational center frequency selection and/or the digital baseband signal used at each frequency to notch out particular bands.

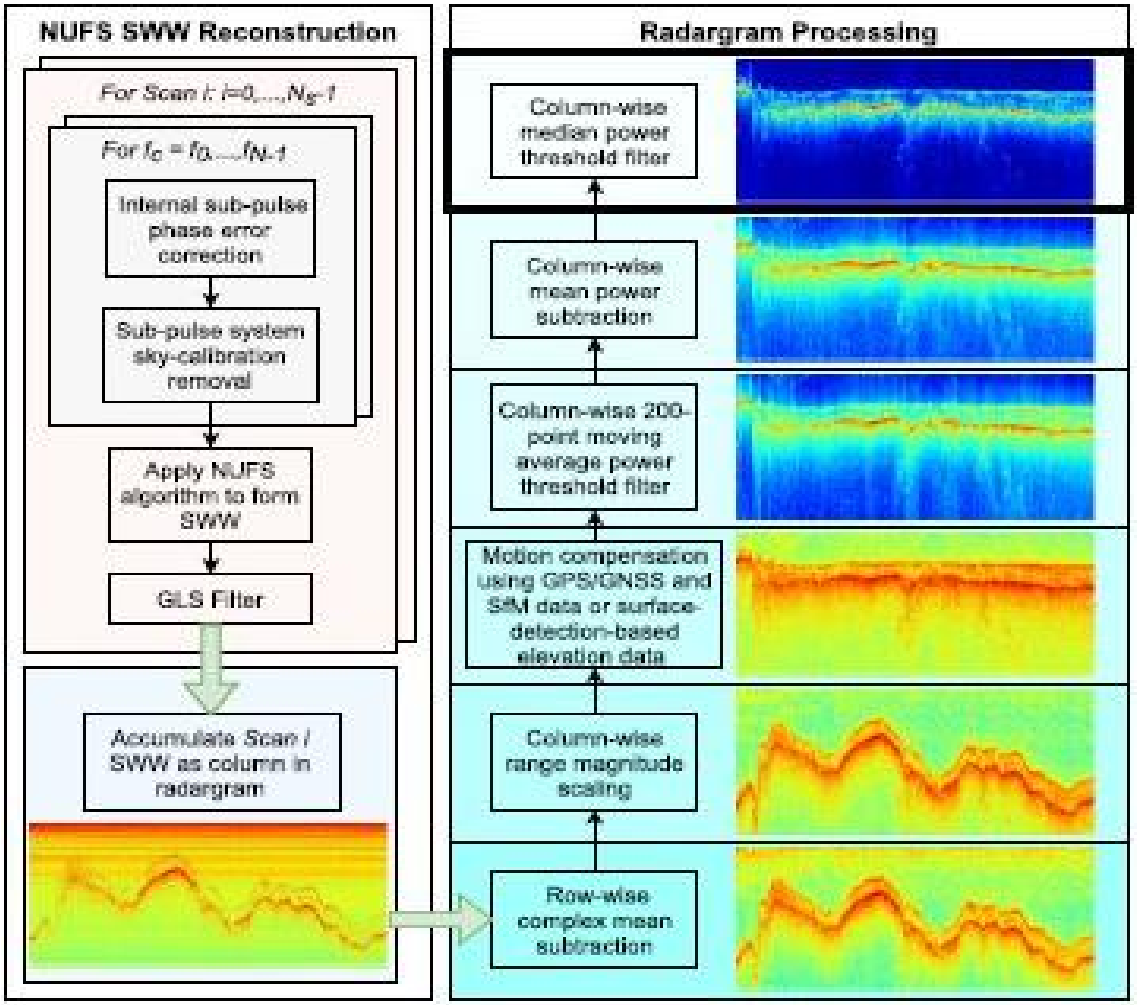

Figure 4. Radar processing diagram showing SWW synthesis using (Left) NUFS algorithm and the radargram processing steps used to compensate UAV platform motion and to reduce background noise and speckle.

We express the discrete-time SWW reconstruction from N received discrete baseband subpulse signals $z[t]$ that are reflected by some point target at range R_s and sampled at rate f_s. At each stepped center frequency f_n, interrogating transmits waveform ω_t of length $T_p$is coherently transmitted at center frequency f_n. We introduce $L = f_s \cdot T_p$ as the number of subpulse samples and $f_n$as the center mixing

$$Z_n[t] = \omega\left[t - \frac{2R_s}{c}\right] e^{-j2\pi f_{\mathrm{n}} \frac{2R_s}{c}} e^{j\emptyset_{\varepsilon,\mathrm{n}}} \tag{3}$$

frequency for subpulse n

We include a random but measurable phase error term $\phi_{e,n}$ to account for any phase imparted through mixing with the LO during signal up/down conversion. We, thus, define the nth subpulse phase- coherent matched filter response $v_n[t] = \omega[t]\, e^{j\phi e,n}$.

Following the SWW reconstruction method described in [36], we compress $z_n[t]$ with $v_n[t]$ at baseband to obtain the series of compressed subpulses $d_n[t] = z_n[t] * v_n[-t]$ that have the discrete Fourier transform (DFT) $D_n[f] = Z_n[f]V^*[f]$. For each subpulse in the frequency domain, we then: 1) apply a BW B_s bandpass filter; 2) upsample to length $L_{up} \geq N\,x$ L via spectrum zero-padding; and 3) frequency shift by Δf_n [36]. Subpulses are then accumulated in the frequency-domain SWW $D[f]$

$$D[f] = \sum_{n=0}^{N-1} D_n[f - \Delta f_n]\, rect\left[\frac{f-\Delta f_n}{B_s}\right] \tag{4}$$

The time-domain compressed SWW $d[t]$ is then computed by taking the inverse discrete Fourier transform (IDFT) of $D[f]$.

The chief limitation of the SWW is the presence of signal-contaminating grating lobes, whose impulse-like shape is due to periodic discontinuities in the SWW spectrum. It has been shown that, by spacing subpulses at nonuniform frequencies, the energy in the grating lobes is spread out in the resulting nonuniform SWW (NU-SWW) [41]–[43]. We note that the NUFS method described in the following section inherently introduces nonuniformity into the SWW spectrum, even when the underlying frequency step sizes are uniform. Other work has been done on active grating lobe cancellation and filtration [36].

B. Nonuniform Nonlinear SWW

In this section, we expand upon work previously reported in [39].

We extend the NU-SWW and nonlinear frequency modulated (NLFM) waveform design [39], [44], [45] to a novel nonuniform nonlinear SWW (NU-NLSWW). The approach to the waveform design is given as follows.

1) Consider an ultrawideband frequency modulated (FM) waveform with a desired power spectral density (PSD) and autocorrelation function.

2) Compute time-domain frequency function corresponding to this ultrawideband FM waveform.

3) Splice the time-domain frequency function at nonuni-form intervals with offsets from a nominal interval Δf chosen randomly from a uniform distribution to construct a set of limited-BW FM subpulses.

To reconstruct the NU-NLSWW waveform from narrow-band subpulses, we propose an extension of the FS algorithm [36] summarized in Section IV-A that introduces a cost function $C_n[f]$ of the form

$$C_n[f] = \min_{f_0,\ldots,f_{L-1}} \sum_{i=0}^{L-1} \left(k_{n,1} \| D_{n+1}[f_i] - D_n[f_i] \|_2^2 + k_{n,2} \left\| \frac{\partial D_{n+1}[f_i]}{\partial f} - \frac{\partial D_n[f_i]}{\partial f} \right\|_2^2 \right) \; s.t. \{ \Delta f_n + \Delta f/2 - \zeta \le f_i \le \Delta f_n + \Delta f/2 + \zeta \} \tag{5}$$

to be minimized in order to find an optimal reconstruction. Here, ζ is a constraint factor that controls the extent of the search, kn,1 and kn,2 are empirically selected weight factors, and $D_n[f]$ is the Fourier transform of the nth subpulse matched filter output. The cost function incorporates the magnitude and first-order derivative of the subpulse spectra in order to maximize smoothness of adjacent subpulse spectra. The subpulses are then stitched together at the minimizing frequencies f_n

$$\widetilde{f_n} = argmin_{f_0,\ldots,f_{L-1}} C_n[f] \tag{6}$$

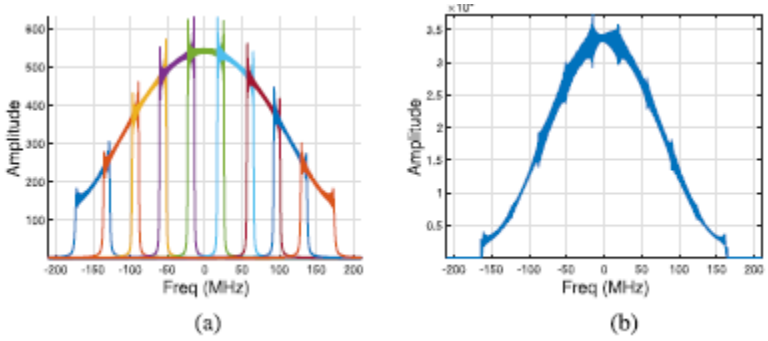

Figure 5. NU-NLSWW spectrum synthesis for 350 MHz total NU-NLSWW BW, N 9 subpulses, and Hamming window weighting (a) NU-NLSWW subpulse spectra. (b) Reconstructed NU-NLSWW.

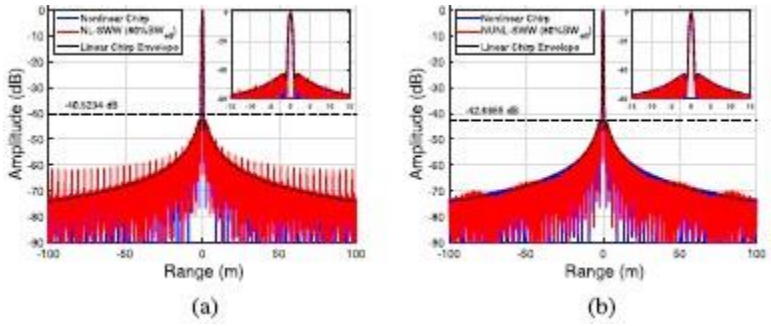

Figure 6. Reconstruction of nonlinear SWWs using (a) existing FS algorithm and (b) new NUFS algorithm. PSL is shown as dashed line.

Because the algorithm searches for nonuniform optimal stitching seams in the subpulses rather than naively stacking them, we refer to this approach as NUFS. The reconstructed NU-NLSWW $D[f]$ then becomes

$$D[f] = \sum_{n=0}^{N-1} D_n[f - \Delta f_n]\, \mathbf{1}_{\tilde{f}_n \le f < \tilde{f}_{n+1}} \tag{7}$$

where $\mathbf{1}_{a \le f < b}$ represents a function of f that is 1 over the interval $a \le f < b$ and 0 elsewhere.

This NUFS algorithm is then used to directly form an NU-NLSWW from the stepped frequency NLFM subpulses, which has the desired spectral and sidelobe characteristics and constant amplitude. The results of this waveform design and BW synthesis method are shown in Fig. 5 for a Hamming window weighting. The individual NLFM subpulse spectra are shown in Fig. 5(a). The NU-NLSWW spectra reconstructed using the newly developed NUFS method are shown in Fig. 5(b). The resulting NU-NLSWW autocorrelation functions along with the equivalent wideband NLFM and LFM chirp waveforms and the peak sidelobe level (PSL) are plotted in Fig. 6(b).

A comparison of the autocorrelation properties of the non-linear SWW (NL-SWW) obtained using the FS reconstruction algorithm proposed in [36] and described in Section IV-A is compared with the new method in Fig. 6 for an NLFM Hamming weighting. In this case, a 350-MHz BW nonlinear constant amplitude SWW is synthesized from N = 9NLFM subpulses using 80% BW eficiencies. The proposed method is shown to substantially reduce grating lobe contamination in the SWW without any additional grating lobe suppression (GLS) processing. We note, however, that the application of the GLS

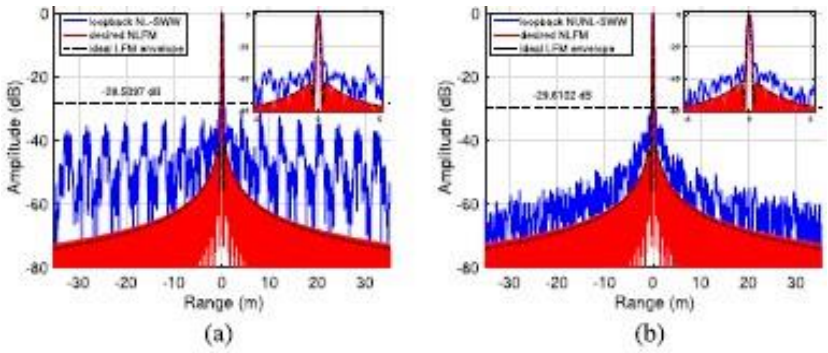

Figure 7. 1-GHz BW NU-NLSWW reconstructed from N 26 subpulses obtained using USRP SDRadar hardware in loopback configuration [39]. PSL is shown as dashed line. (a) Existing FS method. (b) New NUFS method.

GLS filter, as described in [36], remains a useful technique for shaping the received SWW signal spectrum, particularly when the transmitted signal spectrum is notched to avoid specific bands.

We validate the proposed NLFM waveform design and NUFS SWW reconstruction methods in hardware by synthesizing a 1-GHz BW NL-SWW ($N = 26$ subpulses) with a Hamming weighted spectrum at 80% BW efficiency. We use a stepped frequency SDRadar implemented in USRP E312 hard- ware, which has 50 MHz of instantaneous BW. The results of the hardware loopback test are shown in Fig. 7. The results match expectations from simulations and show a substantial reduction in grating lobe level. We note that, for a total desired BW BW_t, $N \approx ceil[BW_t/(B_i \, x \, BW_{eff})]$,where B_i is the subpulse BW and BW_{eff} is the desired BW efficiency. However, because of the random nature of the nonuniform time-domain frequency function splicing, the actual value of N may vary by ±1.

V. Experimental Design and Results

We performed a field campaign at Cameron Pass, Colorado, in March 2020 to evaluate the proposed SDRadar system against independent ground-based observations of snow depth. The SDRadar was mounted on a hexacopter UAV as a snow penetrating radar sensor payload capable of high-resolution subsurface imaging using the NUFS synthetic wideband and signal processing techniques described in Section IV. Two transects were flown: a snow-covered meadow ("Meadow Transect") in the southern part of the test area and a forested area ("Forest Transect") in the northern part of the test area, as shown in Fig. 8(a). A total BW of 1 GHz is synthesized from the 600–1600-MHz band, and a BW efficiency of 80%was empirically selected to minimize the number of frequency steps while still having sufficient subpulse overlap for good NUFS reconstruction characteristics. In addition, ten subpulses are averaged coherently at each step to improve SNR by 10 dB. The total $N = 26$ sweep time is 0.5 s and is linearly dependent on the number of frequency steps (∼.018 s/step). The UAV flight speed was 1 m/s, giving a horizontal resolution of 0.5m, and the nominal output power was ≤10 dBm. The radar sweep PRF is limited by the relatively slow frequency tuning time of the USRP E312 hardware and the 10 pulse averaging. In practice, the UAV flight speed must be slow enough such that the scene remains coherent throughout the frequencysweep. Faster flight speeds may be achieved by reducing the total synthesized BW, which is run-time configurable.

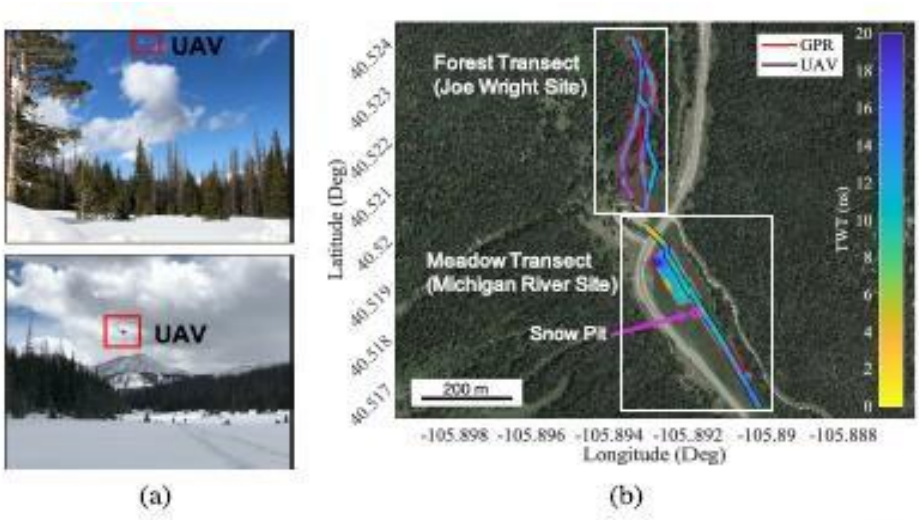

Figure 8. (a) Photographs of (Top) forest and (Bottom) meadow snowfield transects. (b) GPS positions of sled GPR and UAV-SDRadar along both transects for the March 2020 field campaign at Cameron Pass, Colorado. The snowpack TWT measurements made by each system a re illustrated. Note that the flight path of UAV deviates from the sled GPR path by varying distances for both transects because of imperfect flight control systems and terrain obstacles. Satellite imagery obtained from Google Maps API [46].

As a means of validation, we measured the snow depth TWT using a sled equipped with a commercial Sensors and Software pulse EKKO GPR system with 1-GHz antennas and Emlid RS2 GNSS receivers [47]. The postprocessed GNSS locations of the ground-based GPR and the UAV SDRadar for the two transects flown are shown in Fig. 8(b). Also shown in Fig. 8(b), the TWT measurements are made by each system. The methodology used to obtain these results and their analysis are described in detail later in this section.

A. Snow and Ground Surface Detection Algorithm

We develop custom snow and ground surface detection algorithm to track the radar backscatter signatures of both the air/snow interface and the snow/ground interface observed by the UAV-SDRadar.

Of the existing retracking algorithms used to detect surface returns in altimetric systems, the cubic spline retracking algorithm is often cited as having the best performance [48], [49]. However, these 1-D approaches are designed for high-altitude space and airborne systems with wide swaths. They are not sufficient for small UAV subsurface imaging radar systems flying at low altitudes, as the surface backscatter may vary substantially in power. This is due to large fluctuations in platform altitude relative to the platform height above the ground as dictated by the fundamental radar equation [8]. This is further complicated when flying over forested or densely vegetated areas due to the sporadic presence of scattering objects very close to the radar sensor. As such, a 1-D approach to surface detection will easily lose track of the surface interface when the signal is weak or obstructed, producing erratic results.

To this end, we developed a neighbor-aware approach to surface tracking that incorporates independent sensor data from a LiDAR altimeter and GNSS/GPS receiver, as well as the expected continuity and gradient characteristics of the ground and snow surfaces over small spatial scales.

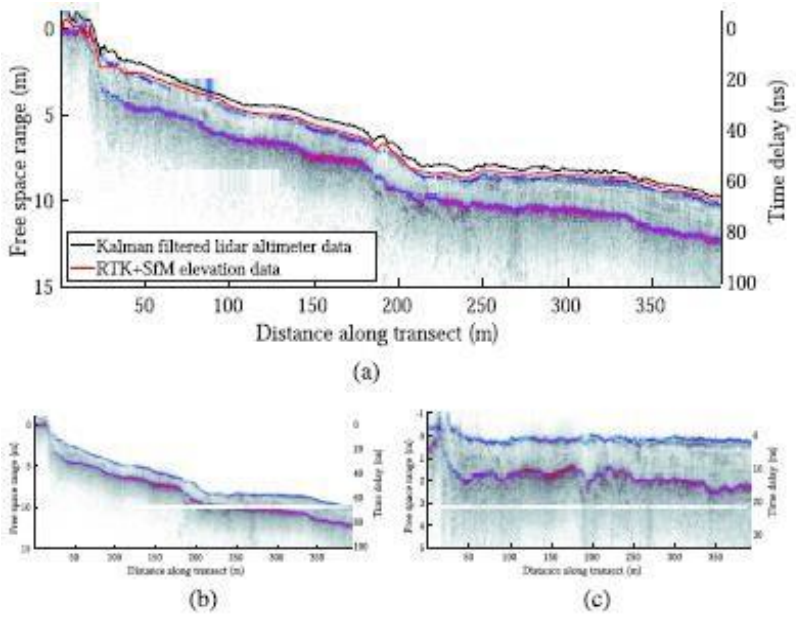

Figure 9. Meadow Transect radargrams before and after surface topography removal. Detected snow surface and ground layers are colorized in the grayscale radargram images with blue tones indicating weaker reflections and red tones indicating stronger reflections. The ground and surface detections are produced by the algorithm described in Section V-A. (a) Radargram after RTK GNSS/GPS UAV elevation correction showing the meadow snow surface topography. Also shown are the Kalman filtered LiDAR altimeter data and independent 1-cm/pixel SfM-MVS-derived elevation data, both corrected for RTK GNSS/GPS UAV elevation. (b) Before surface topography removal.(c) After surface topography removal (using independent SfM data).

The proposed snow and ground surface detection algorithm is described completely in Appendix B.

Fig. 9. Meadow Transect radargrams before and after surface topography removal. Detected snow surface and ground layers are colorized in the grayscale radargram images with blue tones indicating weaker reflections and red tones indicating stronger reflections. The ground and surface detections are produced by the algorithm described in Section V-A. (a) Radargram after RTK GNSS/GPS UAV elevation correction showing the meadow snow surface topography. Also shown are the Kalman filtered LiDAR altimeter data and independent 1-cm/pixel SfM-MVS-derived elevation data, both corrected for RTK GNSS/GPS UAV elevation. (b) Before surface topography removal.(c) After surface topography removal (using independent SfM data).

The results presented herein for the Meadow Transect were obtained entirely using this detection algorithm. For the Forest Transect, which suffers from substantial speckle and poor LiDAR data because

of interference from the canopy, 80 manually selected anchor points were added prior to the second iteration to assist the algorithm. Although easy for the human brain, the problems of noisy/broken edge detection and curve tracing represent an active area of research in the field of computer vision and, while highly important, is not the primary focus of this article [50]–[52]. Rather, we focus on the performance potential of the described UAV-SDRadar system in measuring physical parameters.

B. UAV Elevation-Corrected Radargrams Using GNSS

Following ultrawideband synthesis and filtering of the stepped frequency SWW, we correct for the UAV altitude using data collected by an onboard Emlid Reach M2 real-time kinematic (RTK)/postprocessing kinematic (PPK) L1/L2 GNSS/GPS unit. Each column of the SWW radargrams shown in Figs. 9 and 10 is fractionally shifted via application of a linear phase in the spectral domain in accordance with fundamental Fourier transform theory to compensate for the UAV altitude, and the vertical axis is relative to the snow surface at the beginning of each transect. With the UAV platform altitude removed, the radargrams shown in Figs. 9(b) and 10(b) are representative of the snow/ground surface topography present at the Meadow and Forested transects, respectively. We note that, in the Forested Transect, trees were present throughout, and scattering from the forest canopy is responsible for the increased speckle above the snow surface in Fig. 10, although we note that, at the L-band frequencies used, scattering due to the forested vegetation is relatively weak, and radar signals penetrate the forest canopy effectively as demonstrated herein. In addition, a large tree, which forced the UAV to abruptly gain altitude, is responsible for the feature at ~360 m along the transect in Fig. 10. We note that the feature is primarily due to the abrupt elevation change causing errors in the UAV position estimation rather than scattering from the tree itself.

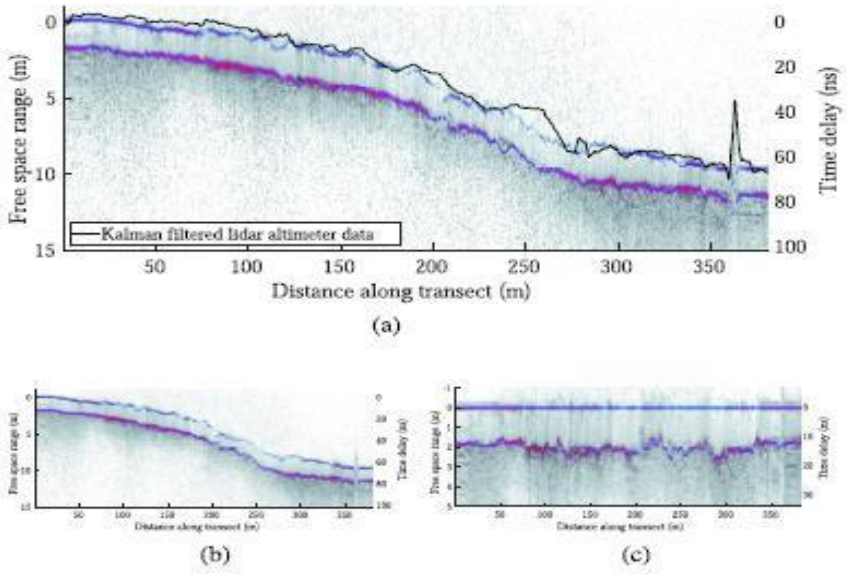

Figure 10. Forest Transect radargrams before and after surface topography removal. Detected snow surface and ground layers are colorized in the grayscale radargram images with blue tones indicating weaker reflections and red tones indicating stronger reflections. The ground and surface detections are produced by the algorithm described in Section V-A. (a) Radargram after RTK GNSS/GPS UAV elevation correction showing the forest snow surface topography. Also shown is the Kalman filtered LiDAR altimeter data corrected for RTK GNSS/GPS UAV elevation. (b) Before surface topography removal.(c) After surface topography removal (using surface detection algorithm).

UAV-based SfM-MVS surveys were conducted at the field study site with ground control points in the Meadow Transect area as part of an ongoing independent effort. The SfM-MVS surveys were conducted with a DJI Mavic 2 Pro drone that flew at 60 m above ground level (AGL) with 75% front and side overlap. Drone imagery was processed in Agisoft Metashape using a workflow comparable to [33]. For the Meadow Transect, we use a 1-cm/pixel resolution SfM snow surface elevation product generated from the multiangle SfM imagery of the field site to correct for surface topography.

The SfM-derived surface elevation data and the Kalman fil-tered altitude data obtained from the onboard LiDAR altimeter are plotted for the Meadow Transect in Fig. 9(a). The SfM elevation data were retrieved from a georeferenced map using the RTK GNSS coordinates of the UAV platform. For each UAV position, all SfM data within a 0.5-m radius footprint (FP) were considered. We also averaged the closest values within a 5-cm radius FP. The values shown were the average of the minimum 10% values within the 0.5-m FP. This was done to isolate points corresponding to the snow surface rather than vegetation or other objects. For the Meadow Transect, both the LiDAR altimeter and SfM map provide good estimates of the snow surface elevation. For the Forest Transect, the LiDAR altimeter data, even after extensive processing and Kalman filtering, are contaminated substantially by the dense foliage and forest canopy, as seen in Fig. 10(a). SfM-based surface elevation data were only provided for the Meadow Transect, as the

primary study area of the SfM survey did not cover the Forest Transect. Furthermore, conducting SfM surveys of heavily forested areas presents substantial challenges because of canopy opaqueness at optical frequencies [12].However, the RF signal transmitted by the UAV-SDRadar is able to effectively penetrate the forest canopy, with backscatter from both the snow surface and ground below clearly detected.

Accordingly, for the Meadow Transect, where the independent elevation sensors provide reliable data, we correct for surface topography using SfM data, as shown in Fig. 9(c). For the Forest Transect, however, we correct snow surface topography directly using the output of the surface estimation algorithm described in Section V-A, as shown in Fig. 10(c). In both cases, the TWT results are derived from the ground and snow surface estimated by the proposed surface estimation algorithm. Noncolorized versions of the radargrams can be found in Appendix C.

C. Comparison with Ground-Based GPR

Using the algorithm described in Section V-A, we obtain the UAV-SDRadar TWT measurements by taking the difference of the ground and snow surface detections and compare them with the ground- based commercial GPR measurements. As shown in Fig. 8(b), the flight path of the UAV deviates from the ground-based sled GPR path by varying amounts for both transects. Furthermore, differences in spatial sampling rate and radar FP size necessitate a normalization of the datasets for meaningful comparison.

Given the set of GPR TWT measurements, T^{gpr} where the GPS/GNSS-derived position of the GPR is $p^{gpr} = [x^{gpr}, y^{gpr}, 0]$ for GPR scan j, we compute a weighted sum of all GPR measurements falling within a given diameter FP (FP) of the UAV-SDRadar at the GPS/GNSS-derived platform position $p^{uav} = [x^{uav}, y^{uav}, z^{uav}]$ for each UAV-SDRadar scan i. Based on the radar received power,

which, for a point target at range R is proportional to 1/R4, we arrive at the following weighting scheme to compute the weighted average of GPR TWT measurements in the ith UAV-SDRadar FP, T^{gpr}:

$$\omega_{i,j} = \left(\frac{z_i^{uav}}{\left\| p_i^{uav} - p_j^{gpr} \right\|_{l2}} \right)^4 \forall\ j : \sqrt{\left(x_i^{uav} - x_j^{gpr} \right)^2 + \left(y_i^{uav} - y_j^{gpr} \right)^2} \leq FP/2 \qquad (8)$$

$$T_i^{gpr} = \frac{\sum_j \left(\omega_{i,j} \cdot T_j^{gpr} \right)}{\sum_j \omega_{i,j}} \qquad (9)$$

Using the weighting scheme described in (8), we compare the GPR and UAV-SDRadar measurements for four FP sizes FP $\in \{20, 10, 5, 2\}$ corresponding to the diameter of a circular FP on the ground in meters. The along-profile survey results showing the TWT measurements are shown for both transects in Fig. 11.

Scatter plot representations of the TWT data, with horizontal and vertical axes corresponding to GPR and UAV-SDRadar values, respectively, are presented in Fig. 12 for multiple UAV-SDRadar FP sizes.

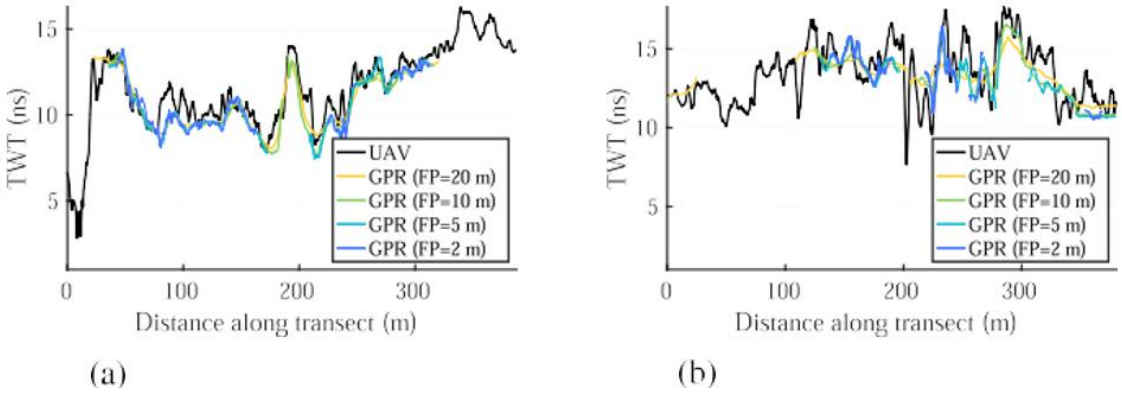

Figure 11. Along-profile comparison of GPR and UAV-SDRadar TWT results. The weighted average is taken over all nearest neighbor GPR measurements falling within a given FP size centered around each UAV lat/lon GNSS coordinate, as described in (8). The FP size refers to the diameter of a circle on the ground surface (see also Fig. 12). (a) Meadow Transect. (b) Forest Transect.

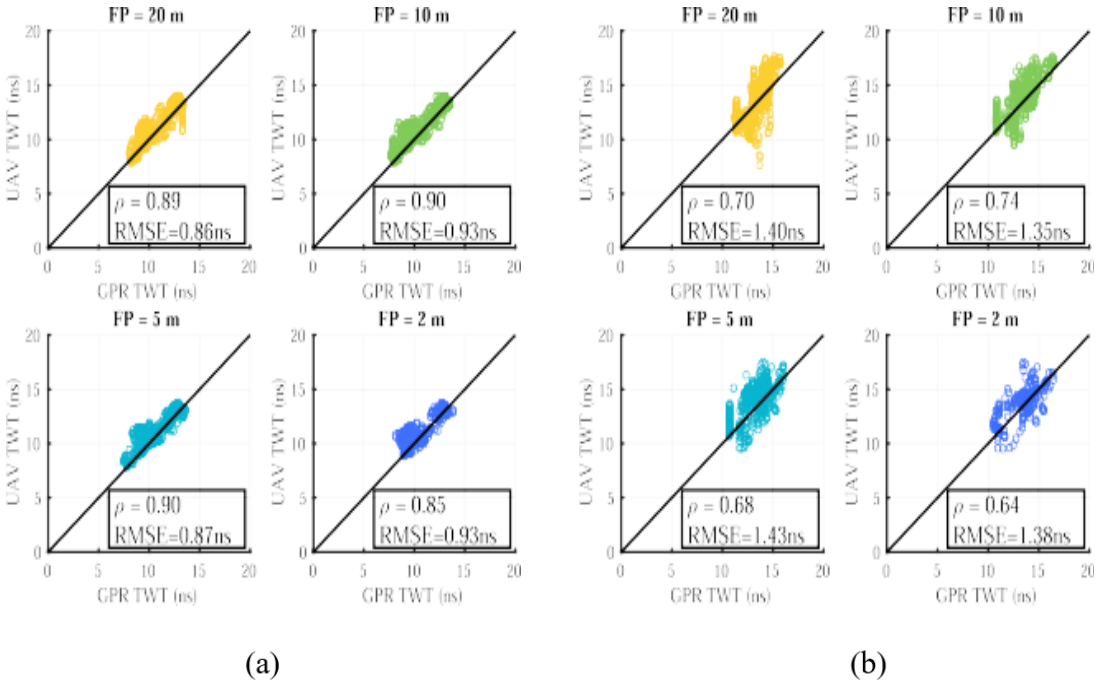

Figure 12. Scatter plot comparison of GPR and UAV-SDRadar TWT results for different FP sizes. The weighted average is taken over all nearest neighbor GPR measurements falling within a given FP size centered around each UAV lat/lon GNSS coordinate, as described in (8). The FP size refers to the diameter of a circle on the ground surface (see also Fig. 11). (a) Meadow Transect. (b) Forest Transect.

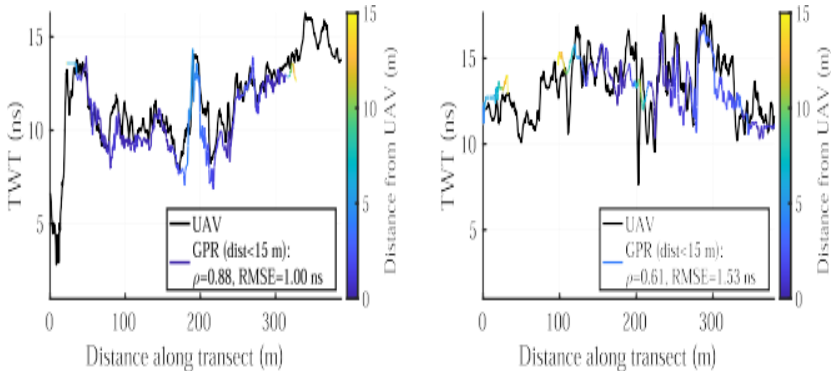

(a) (b)

Figure 13. Along-profile comparison of UAV-SDRadar TWT measurements with the nearest GPR measurement for a given UAV lat/lon GNSS coordinate. The distance of the closest GPR data point from the corresponding UAV data point is indicated by line color. GPR data points that are farther than 15 m away from the UAV position are not considered (see also Fig. 14). (a) Meadow Transect. (b) Forest Transect.

In Fig. 13, we provide along-profile comparisons of the UAV-SDRadar TWT with the closest GPR TWT within 15 m (or equivalently, within a 30-m-diameter FP) of the UAV-SDRadar platform for the corresponding measurement. Scatter plot representations of the TWT data, with horizontal and vertical axes corresponding to GPR and UAV-SDRadar values, respectively, are presented in Fig. 14 for the closest GPR measurement.

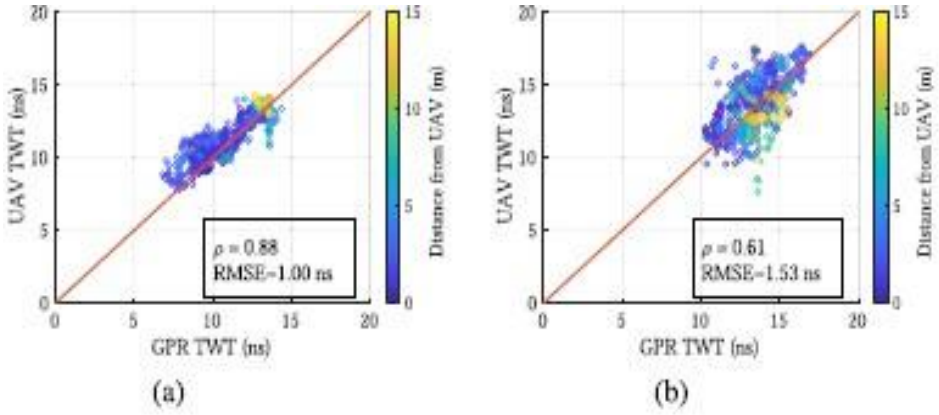

Figure 14. Scatter plot comparison of GPR TWT measurement closest to the UAV for a given position. The distance of the closest GPR data point from the corresponding UAV data point is indicated by color. GPR data points that are farther than 15 m away from the UAV position are not considered (see also Fig. 13). (a) Meadow Transect. (b) Forest Transect.

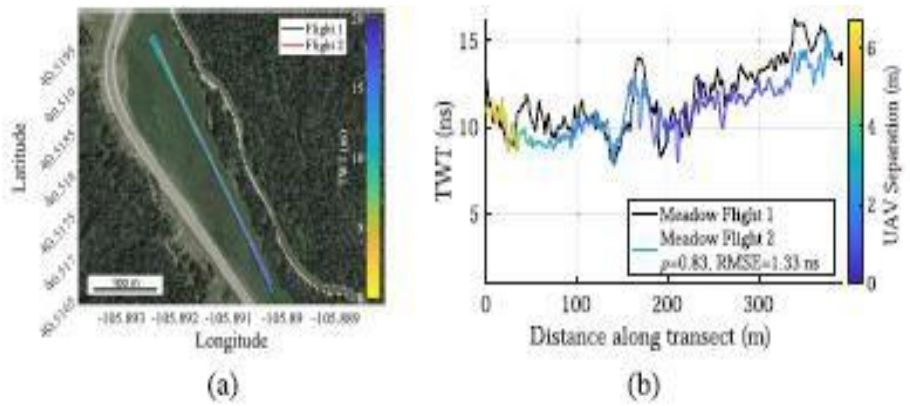

Figure 15. Repeated Meadow Transect flights. (a) Flight paths. (b) TWT measurements.

To demonstrate the repeatability of measurements, the Meadow Transect was flown twice. A comparison of the first and second meadow flight paths and measured TWT is given in Fig. 15(a) and (b), respectively. The correlation coefficient between the two flights is 0.83 with a root mean square error (RMSE) of 1.33 ns. We note that the actual flight paths diverge because of changing weather conditions and imperfect sUAS flight controls.

We report the statistical comparison between the UAV-SDRadar and GPR measurements in Tables 3-5 for the first Meadow, second Meadow, and Forest Transects, respectively. For the four FP sizes and the closest measurement comparisons, we report RMSE, correlation coefficient (ρ), and unbiased Nash-Sutcliffe efficiency (NSE), as well as the number of GPR measurements considered NGPR in each case. All results are statistically significant with p-values < 0.001 for the Meadow and Forest Transects. A snow dielectric of 1.41 is used in these statistics based on measurements taken at a snow pit (see Section V-D). The lower correlation of the Forest Transect data is explained by: 1) scattering of the signal by forest canopy; 2) higher flight altitude of UAV AGL to avoid trees resulting in lower SNR; and 3) divergence of the UAV path from the ground-based GPR path, as shown in Fig. 8(b).

Table 3. Statistical Comparisons of TWT estimated by UAV SDRadar with Ground-Based GPR Measurements along the Meadow Transect. *Assuming a Snow Dielectric of 1.41

Parameter	Footprint Size (m)				
	20	10	5	2	closest
RMSE (ns)	0.86	0.93	0.87	0.93	1.00
RMSE (cm)*	10.81	11.76	10.97	11.75	12.60
Corr. ρ	0.89	0.9	0.9	0.85	0.88
Bias (ns)	0.44	0.60	0.51	0.53	0.49
Unbiased NSE	0.77	0.81	0.81	0.73	0.77
N_{GPR}	533	496	434	314	548

Table 4. Statistical Comparisons of TWT estimated by UAV SDRadar with Ground-Based GPR Measurements along the Second Meadow Transect. *Assuming a Snow Dielectric of 1.41

Parameter	Footprint Size (m)				
	20	10	5	2	closest
RMSE (ns)	0.82	0.88	0.84	0.93	1.16
RMSE (cm)*	10.32	11.06	10.66	11.81	14.64
Corr. ρ	0.82	0.8	0.8	0.79	0.75
Bias (ns)	-0.02	0.1	-0.12	-0.11	0.02
Unbiased NSE	0.67	0.64	0.64	0.61	0.55
N_{GPR}	589	512	439	122	605

Table 5. Statistical Comparisons of TWT estimated by UAV SDRadar with Ground-Based GPR Measurements along the Forest Transect. *Assuming a Snow Dielectric of 1.41

Parameter	Footprint Size (m)				
	20	10	5	2	closest
RMSE (ns)	1.40	1.35	1.43	1.38	1.53
RMSE (cm)*	17.74	17.05	18.06	17.42	19.28
Corr. ρ	0.7	0.74	0.68	0.64	0.61
Bias (ns)	0.29	0.55	0.62	0.34	0.20
Unbiased NSE	-0.59	0.24	0.23	0.26	-0.012
N_{GPR}	527	433	359	192	564

D. Snow Pit (Michigan River)

The UAV-SDRadar collected 202 measurements with a total synthesized BW of 1.5 GHz across the 600–2100-MHz frequency bands while hovering over a snow pit located near the Meadow Transect at the Michigan River Site, as marked on the map in Fig. 8(b).

Two relative dielectric permittivity profiles were measured at the snow pit, which had a depth of 115 cm at the profile measurement points. The average snow depth measured at eight points around the perimeter of the pit was 120.9cm (σ = 4.4 cm). Dielectric measurements were made using a WISe Snow liquid water content sensor from A2 Photonic Sensors. In Fig. 16, we compare the average radar backscatter with the measured dielectric profiles and the gradient of the dielectric profiles. We use the average relative snow pit dielectric $\bar{\epsilon}_r = 1.41$ to determine the electromagnetic wave propagation velocity $\upsilon = c/\sqrt{\bar{\epsilon}_r}$ and, thus, to estimate the snow depth from the radar signal TWT measurements as 125.2cm (σ = 12.6 cm). As shown in Fig. 16, the UAV-SDRadar accurately measures the ground-truth depth of the snow at the snow pit to within 4.4 cm. Furthermore, changes in the dielectric gradient, which appear as stratigraphy in the photograph of the snow pit, are present as peaks in the radar backscatter signal.

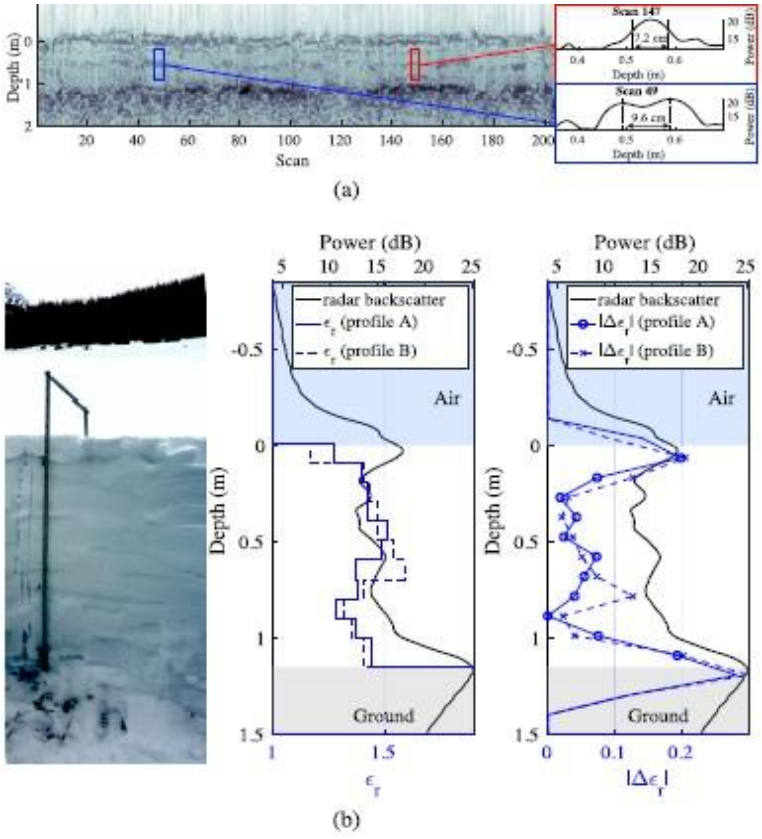

Figure 16. Snow pit measurement results. The snow pit has a ground truth snow depth of 120.9 cm and average dielectric permittivity $\bar{E}_r$ 1.41. The radar backscatter is the average of 202 radar scans. Dielectric profiles A and B were taken at different locations in the snow pit. The average depth estimated by the UAV-SDRadar is 125.2 cm. (a) Radargram collected as UAV-SDRadar hovered over snow pit. (b) Snow pit profile showing a photograph of (Left) snow pit wall, (Center) Measured dielectric profiles E_r , and (Right) dielectric gradient magnitude $|L\text{-}E_r|$ compared with the measured radar backscatter.

The theoretical radar resolution is $r = {}^{c}/_{(2^{*}\,BW\sqrt{\epsilon_{\mathrm{r}}}\;)}$. Thus, for the 1.5-GHz BW SWW in the snow with dielectric 1.41, we expect depth resolution performance of 8.4cm. To assess the resolution achieved by the UAV-SDRadar for imaging subsurface layering, we examine two metrics: 1) the –3-dB peak width of a single subsurface layer reflection and 2) the separation between two adjacent subsurface reflections. In Fig. 16(a), scan 147 of the radargram features a subsurface reflection at 0.55 m. The –3-dB peak width of this reflection is 7.2 cm. Scan 49 features two close but distinct reflections separated by a null that is 2.8 dB down from the stronger of the two peaks. The separation of the two peaks is 9.6cm.This demonstrates that the UAV-SDRadar is capable of measuring not only snow depth but also that the sensor has high enough resolution and sensitivity to measure subsurface layering in the snow at the expected theoretical performance.

VI. Discussion

The quality of the LiDAR altimetry data plays a substantial role in determining the ease with which the UAV altitude AGL (and, therefore, the snow surface) can be estimated. When the UAV is flying slowly over open terrain unobstructed by foliage, the LiDAR altimetry data were very reliable and well-aligned with the snow surface reflection seen in the radargram. When this is not the case, the snow surface must be estimated to a greater degree directly from features present in radargram and possibly with human assistance. It is expected that, as this research area matures, better performing surface and feature detection algorithms, particularly those using machine-learning-based approaches, will emerge. Because of the dry snowpack present at the studied sites, the reflection from the air–snow interface is substantially weaker than that from the snow-ground interface at the frequency range used in our observations. This added difficulty to the detection of the snow surface and required the surface detection algorithm to be tuned with this knowledge a priori.

In environments with wetter snow, the radar reflection from the snow surface might be stronger than that from the ground below. This may be due to: 1) the increase in dielectric contrast between the air and snow (and potential decrease in dielectric contrast between the snow and ground) and 2) the increased attenuation of the radar signal through the snow because of higher water content [53]. For the results presented, the snow surface was more difficult to identify in the radar signal than the ground surface.

However, in the case of wet snow, the opposite may be true. In such cases, the proposed surface detection algorithm would have to be modified according to the expected relative strength of the returns. A more general broken-edge surface detection algorithm that can identify not only snow and ground surfaces but also identify an arbitrary unknown number of subsurface layers is desirable. Machine-learning-based approaches have shown promise for solving such problems [52], [54], [55], but further investigation of their application in low-altitude UAV-based radar imaging problems is necessary.

What is shown in both the UAV-SDRadar and GPR data in Section V is that spatial variability (along a transect) can be high in some areas, with TWT differences >5 ns observed over the span of a few meters and low in others with near-constant TWT across over tens of meters. It stands to reason that the spatial variability of snow depth across areas where the paths taken by the UAV and GPR diverge would exhibit similar characteristics as those observed along the measured transects. Therefore, in addition to the naturally expected cases where small offsets yield small measurement differences and vice versa, we expect to see both cases where the UAV-SDRadar and GPR produce different measurements for small spatial offsets of only a few meters and cases where they produce similar measurements for spatial offsets exceeding 10 m. These areas of variability may be due to changes in snow surface topography (wind slab,

sun cups, and so on), ground topography or features (boulders, downed logs, and so on), or the electromagnetic structure of varying subsurface features (wind slabs, the preferential flow of meltwater within the snowpack, the presence of vegetation, and so on). Therefore, when interpreting the results, it is important to consider both the measurements obtained by each instrument and the relative spatial and topographical information.

Radar sensors, in theory, provide an obvious and complementary solution to the limitations of optical sensors (i.e., LiDAR and SfM-MVS) for measuring snow depth. The lower frequency radar signals are able to penetrate not only foliage and forest canopy cover but also snow layers and can produce depth profile imagery of a snowpack from a single-pass measurement. Furthermore, because it is possible to estimate material properties from backscattered radar signals using electromagnetic scattering models, it is possible in theory to directly retrieve SWE from a single radar observation [8], [29], [56]– [58]. In such a case, information from multiple frequency bands within the synthesized BW would likely be needed to retrieve the depth-dependent dielectric permittivity profile via electromagnetic inverse scattering techniques, which is the subject of our ongoing work.

Given the historic 2019 avalanche season in Colorado, which leads U.S. states in avalanche fatalities [59], a further application of this research is monitoring snow depth and snow stratigraphy to assist in identifying avalanche-prone regions, which intersects with transportation infrastructures, such as roads and engineered structures. The results could lead to a better understanding of loading patterns of avalanche-prone slopes and allow transportation department maintenance staff and engineers to more effectively optimize and implement a plan of action for unstable slopes and landscapes that can adversely affect transportation corridors. Furthermore, the ability to create snow depth products without having to step onto the slope would substantially increase the safety of avalanche control operations.

Derivatives of this research could include temporal variations in the snow–water volume and snow density that will enhance runoff forecasting related to water-resources planning, flood warnings, and mitigation strategies. Snow depth, snow density, and snow volume are important snow metrics. These metrics are traditionally monitored at sparsely distributed ground-based stations (SNOTEL), using snow pits and probes, and modeled in areas where data are not available. Data from sUAS-based SDRadar would complement these distributed stations by increasing the spatial and temporal distributions of snow variables. Successful completion of the workflow will create a remote sensing, rapid deployment platform for generating snow depth and snow stratigraphy, snow-density, and snow-volume grids at prescribed and repeatable transects. This technology would vastly expand the point observations collected in situ, allow data collection on unsafe, avalanche-prone slopes, and would provide higher spatial resolution than satellite data products, making it a key intermediate link between in situ and satellite observations.

VII. Conclusion

In this work, we have demonstrated the successful use of a novel SWW NUFS algorithm in an ultrawideband SDRadar sensor on a UAV platform to measure distributed snow depth at a field site in Colorado. Using a low-cost COTS USRP SDR-based SDRadar sensor, we have demonstrated tunable coherent ultrawideband radar operation from a moving UAV platform with complete removal of grating lobes and other signal processing artifacts. This is the first successful demonstration of UAV-based radar imaging and retrieval of snow depth in a heavily forested area and the first integration of UAV-based radar, SfM-MVS, and LiDAR altimetry data for snowpack mapping. We have validated the UAV-SDRadar results with ground-based GPR sled measurements, making this the first field campaign with results from UAV-based radar compared with GPR-derived ground truth.

We have also imaged snow layer stratigraphy from a UAV-SDRadar and compared the results with snow pit dielectric measurements. We have shown successful UAV platform motion compensation using RTK/PPK GNSS/GPS sensor and topography compensation using both independent SfM measurements and an original surface detection algorithm that incorporates LiDAR altimetry data and radargram features to identify snow and ground interfaces.

Appendix A – Acronyms and Abbreviations

In Table 6, we provide a list of acronyms and abbreviations used in this work.

Table 6. List of Acronyms

Symbol	Description
AGL	Above Ground Level
AWG	Arbitrary Waveform Generator
BW	Bandwidth
CA-CFAR	Cell-Averaging Constant False-Alarm Rate
COTS	Commercial-off-the-Shelf
DFT	Discrete Fourier Transform
FM	Frequency Modulated
FMCW	Frequency Modulated Continuous Wave
FP	Footprint
FS	Frequency Stacking
GLS	Grating Lobe Suppression
GNSS	Global Navigation Satellite System
GPR	Ground Penetrating Radar
GPS	Global Positioning System
IDFT	Inverse Discrete Fourier Transform
LFM	Linear Frequency Modulated
LO	Local Oscillator
NLFM	Non-Linear Frequency Modulated
NUFS	Non-Uniform Frequency Stitching
NL-SWW	Nonlinear Synthetic Wideband Waveform
NSE	Nash-Sutcliffe Efficiency
NU-SWW	Non-Uniform Synthetic Wideband Waveform
NU-NLSWW	Non-Uniform Nonlinear Synthetic Wideband Waveform
PLL	Phase-Locked Loop
PPK	Post-processing Kinematic
RMSE	Root Mean Square Error
RTK	Real-time Kinematic
RX	Receive
SBC	Single Board Computer
SDR	Software Defined Radio
SDRadar	Software Defined Radar
SfM	Structure from Motion
SfM-MVS	Structure from Motion-Multi-View Stereo
sUAS	Small Unmanned Aircraft System
SWE	Snow Water Equivalent
SWW	Synthetic Wideband Waveform
TWT	Two-way Travel Time
TX	Transmit
UAV	Unmanned Aerial Vehicle
USRP	Universal Software Radio Peripheral
UWB	Ultra-wideband

Appendix B – Snow and Ground Surface Detection Algorithm

The surface detection algorithm for an *N* scan radargram is summarized as follows.

1) Apply moving median with a standard deviation-based 99.87% confidence outlier rejection filter to LiDAR data.
2) Apply the Kalman filter to prefiltered LiDAR data to obtain UAV height AGL estimates L_i for each scan *i*.
3) For each scan Z_i, compute the mean power Z_i,and estimate the leading edge of the radar return Si0, where $a_{zc}, \delta^-, and\ \delta^+$, are empirically derived constants representing the mean scale factor, and the upper and lower bounds on the expected deviation of the LiDAR altimetry data, respectively.

$$S_i^0 = \min_{r_j} r_j \,|\{Z_{i,j} > a_{zc} \cdot \bar{Z}_i, L_i - \delta_{zc}^- < r_j < L_i + \delta_{zc}^+\} \tag{B.1}$$

4) Compute the 11-point ($M = 5$) centered moving average across scans of S_i^0 to obtain $\bar{S}_i^0$

$$\bar{S}_i^0 = \frac{1}{2M+1}\sum_{l=i-M}^{l=i+M} S_l^0 \tag{B.2}$$

5) Estimate the ground surface G_i^0 as the highest peak in the received SWW correlation signa G_i^0

$$G_i^0 = argmax_{i,j} Z_{i,j} |\{r_j > \bar{S}_i^0\} \tag{B.3}$$

6) Estimate the average snow depth $d^0 = \frac{1}{N}\sum_i |G_i^0 - \bar{S}_i^0$

7) Apply a cell-averaging constant false-alarm rate (CA-CFAR) threshold [60] to each SWW scan Z_i to obtain $A_i = CFAR_{CA}(Z_i)$.

8) Compute and store column wise image gradient of the Gaussian filtered radargram ∇y A

where H_5 is a 5 x 5 Gaussian kernel with $\sigma = 1$.

$$\nabla_y A = \begin{bmatrix} 1 & 2 & 1 \\ 0 & 0 & 0 \\ -1 & -2 & -1 \end{bmatrix} * (H_5 * A) \tag{B.4}$$

9) Initialize the ground estimate $\tilde{G}_i^0 = \tilde{S}_i^0 + \tilde{d}_0$ and snow surface estimates as $\tilde{S}_i^0 = \bar{S}_i^0$

10) Define the reward function $P_{i,j}$

$$P_{i,j} = \begin{cases} \frac{1}{11}\left(\sum_{l=j-5}^{l=j+5} A_{i,l}\right) + \max_{j-10<l<j} \nabla_y A_{i,l}, if\ A_{i,j} > A_{i,j-1}\ and\ A_{i,j} > A_{i,j+1}\ otherwise \\ -\infty, \end{cases} \tag{B.5}$$

11) For iteration k:= 1 to 2:

Initialize the snow/ground surface estimates for the first scan $i = 0$

$$\tilde{S}_0^k = argmin_{rj}\alpha_1\left|r_j - \tilde{S}_0^{k-1}\right| - \alpha_3 P_{0,j} \quad \text{(B.6)}$$

$$\tilde{G}_0^k = argmin_{rj}\alpha_1\left|r_j - \tilde{G}_0^{k-1}\right| - \alpha_3 P_{0,j} \quad \text{(B.7)}$$

12) **For each scan i** > 1:

13) Find all peaks within 30 dB of the maximum and compute the cost functions C_j^S and C_J^G for the snow and ground surfaces, respectively.

14) if k == 1

$$C_{i,j}^s = \alpha_2\left|r_j - \tilde{S}_{i-1}^k\right| - \alpha_3 P_{i,j} \quad \text{(B.8)}$$

$$C_{i,j}^G = \alpha_2\left|r_j - \widetilde{SG}_{i-1}^k\right| - \alpha_3 P_{i,j} \quad \text{(B.9)}$$

15) **else**.

16) Estimate three linear least squares (LS) fits: LS_c using 160 points centered around but not including *i*, LS_L using 40 points to the left of *i*, and LS_R using 40 points to the right of *i*. For each, compute the RMSE of the fit

$$C_{i,j}^s = \frac{\left|LS_L - \tilde{S}_i^{k-1}\right|^2}{RMSE_L} + \frac{\left|LS_R - \tilde{S}_i^{k-1}\right|^2}{RMSE_R} + \frac{\left|LS_c - \tilde{S}_i^{k-1}\right|^2}{RMSE_c} - \alpha_3 P_{i,j} \quad \text{(B.10)}$$

$$C_{i,j}^G = \frac{\left|LS_L - \tilde{G}_i^{k-1}\right|^2}{RMSE_L} + \frac{\left|LS_R - \tilde{G}_i^{k-1}\right|^2}{RMSE_R} + \frac{\left|LS_c - \tilde{G}_i^{k-1}\right|^2}{RMSE_c} - \alpha_3 P_{i,j} \quad \text{(B.11)}$$

17) **end if**

$$\tilde{S}_i^k = argmin_{rj}\alpha_1\left|r_j - \tilde{S}_i^{k-1}\right|^k + C_{i,j}^s \quad \text{(B.12)}$$

$$\tilde{G}_i^k = argmin_{rj}\alpha_1\left|r_j - \tilde{G}_i^{k-1}\right|^k + C_{i,j}^G \quad \text{(B.13)}$$

Where $\alpha_1, \alpha_2, and\ \alpha_3$ are empirically derived constant weighting factors.

18) If a manual anchor value is specified for either the ground or surface, use that instead for S_i or $G_i$as appropriate.

19) **end for**

20) Perform cubic interpolation of estimates across scans using the cost function values that are local minima and/or below the median as anchor points.

21) Update snow and ground surface estimates.

22) **end for**

23) Output surface/ground detections are local peaks nearest to interpolated estimates.

Appendix C – Radargrams

In Fig. 17, we provide radargrams prior to RTK GNSS/GPS UAV elevation correction to show the UAV height AGL across the transects. In Fig. 18, we provide RTK GNSS/GPS UAV elevation corrected radargrams without colorization of the detected snow/ground surfaces so that the reader may compare the snow/ground surface pixels selected by the proposed algorithm with the raw radargram.

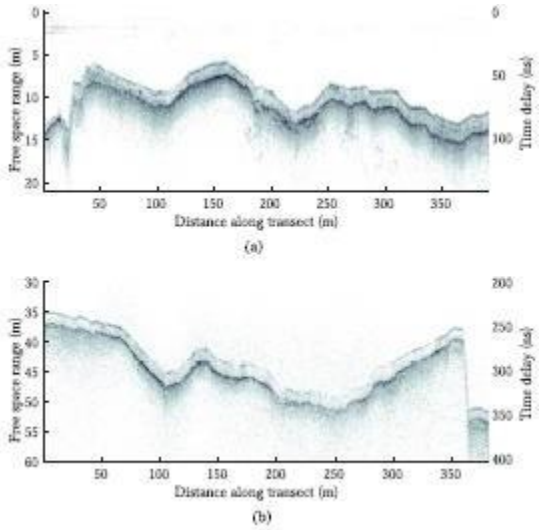

Figure 17. (a) Meadow and (b) Forest Transect radargrams prior to UAV altitude correction showing the altitude of the UAV relative to the snow surface. See also Figs. 9 and 10.

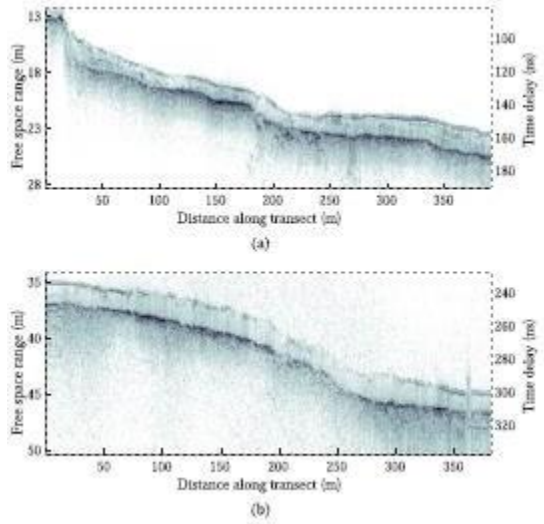

Figure 18. (a) Meadow and (b) Forest Transect radargrams after RTK GNSS/GPS UAV elevation correction showing the snow surface topography and relative to the UAV altitude AGL. See also Figs. 9 and 10.

References

[1] M. Durand et al., “NASA SnowEx science plan: Assessing approaches for measuring water in Earth’s seasonal snow,” Nat. Aeronaut. Space Admin., Washington, DC, USA, Tech. Rep., 2017, p. 68. [Online]. Available: https://snow.nasa.gov/sites/default/files/SnowEx_Science_ Plan_v1.6.pdf

[2] A. Lundberg, N. Granlund, and D. Gustafsson, “Towards automated ‘ground truth’ snow measurements—A review of operational and new measurement methods for Sweden, Norway, and Finland,” Hydrol. Processes, vol. 24, no. 14, pp. 1955–1970, 2010.

[3] R. C. Bales, N. P. Molotch, T. H. Painter, M. D. Dettinger, R. Rice, and J. Dozier, “Mountain hydrology of the western United States,” Water Resour. Res., vol. 42, no. 8, Aug. 2006, Art. no. W08432.

[4] J.I.López-Moreno et al., “Snowpack variability across various spatiotemporal resolutions,” Hydrol. Processes, vol. 29, pp. 1213–1224, Mar. 2015.

[5] K. Elder, J. Dozier, and J. Michaelsen, “Snow accumulation and distribution in an Alpine watershed,” Water Resour. Res., vol. 27, no. 7, pp. 1541–1552, Jul. 1991.

[6] N. Yankielun, W. Rosenthal, and R. E. Davis, “Alpine snow depth measurements from aerial FMCW radar,” Cold Regions Sci. Technol., vol. 40, nos. 1–2, pp. 123–134, Nov. 2004.

[7] E. Arnold et al., “CReSIS airborne radars and platforms for ice and snow sounding,” Ann. Glaciol., vol. 61, no. 81, pp. 58–67, Apr. 2020.

[8] F. T. Ulaby, R. K. Moore, A. K. Fung, and F. T. Ulaby, Microwave Remote Sensing Fundamentals and Radiometry, vol. 1. Norwood, MA, USA: Artech House, 1981.

[9] F. T. Ulaby, R. K. Moore, and A. K. Fung, Microwave Remote Sensing: Active and Passive, vol. 2. Norwood, MA, USA: Artech House, 1986.

[10] D. McGrath et al., “Spatially extensive ground-penetrating radar snow depth observations during NASA’s 2017 SnowEx campaign: Comparison with *in situ*, airborne, and satellite observations,” Water Resour. Res., vol. 55, no. 11, pp. 10026–10036, Nov. 2019.

[11] C. Matzler, “Microwave permittivity of dry snow,” IEEE Trans. Geosci. Remote Sens., vol. 34, no. 2, pp. 573–581, Mar. 1996.

[12] P. Harder, J. W. Pomeroy, and W. D. Helgason, “Improving sub-canopy snow depth mapping with unmanned aerial vehicles: LiDAR versus structure-from-motion techniques,” Cryosphere, vol. 14, no. 6, pp. 1919–1935, Jun. 2020.

[13] A. Tan, K. Eccleston, I. Platt, I. Woodhead, W. Rack, and J. McCulloch, “The design of a UAV mounted snow depth radar: Results of measurements on Antarctic sea ice,” in Proc. IEEE Conf. Antenna Meas. Appl.(CAMA), Tsukuba, Japan, Dec. 2017, pp. 316–319.

[14] R. O. R. Jenssen, M. Eckerstorfer, S. Jacobsen, and R. Storvold, “Drone-mounted UWB radar system for measuring snowpack properties: Technical implementation, specifications and initial results,”

in Proc. Int. Snow Sci. Workshop, 2018, pp. 7–12.

[15] R. O. R. Jenssen, M. Eckerstorfer, and S. Jacobsen, “Drone-mounted ultrawideband radar for retrieval of snowpack properties,” IEEE Trans. Instrum. Meas., vol. 69, no. 1, pp. 221–230, Jan. 2020.

[16] R. O. R. Jenssen and S. Jacobsen, “Drone-mounted UWB snow radar: Technical improvements and field results,” J. Electromagn. Waves Appl., vol. 34, no. 14, pp. 1930–1954, Sep. 2020.

[17] A. E.-C. Tan, J. McCulloch, W. Rack, I. Platt, and I. Woodhead, “Radar measurements of snow depth over sea ice on an unmanned aerial vehicle,” IEEE Trans. Geosci. Remote Sens., vol. 59, no. 3, pp. 1868–1875, Mar. 2021.

[18] M. Stockham, J. Macy, and D. Besson, “Radio frequency ice dielectric permittivity measurements using CReSIS data,” Radio Sci., vol. 51, pp. 194–212, Mar. 2016.

[19] B. Panzer et al., “An ultra-wideband, microwave radar for measuring snow thickness on sea ice and mapping near-surface internal layers in polar firn,” J. Glaciol., vol. 59, no. 214, pp. 244–254, 2013.

[20] J. B. Yan, S. Gogineni, D. Braaten, J. Brozena, F. Rodriguez-Morales, and E. Arnold, “Ultra-wideband radars operating over the frequency range of 2–18 GHz for measurements on terrestrial snow and ice,” in Proc. IEEE Int. Geosci. Remote Sens. Symp. (IGARSS), Beijing, China, Jul. 2016, pp. 7078–7081.

[21] C. Leuschen et al., “UAS-based radar sounding of the polar ice sheets,” IEEE Geosci. Remote Sens. Mag., vol. 2, no. 1, pp. 8–17, Mar. 2014.

[22] W. S. Holbrook, S. N. Miller, and M. A. Provart, “Estimating snow water equivalent over long mountain transects using snowmobile-mounted ground-penetrating radar,” Geophysics, vol. 81, no. 1, pp. WA183–WA193, Jan. 2016.

[23] D. McGrath et al., “Interannual snow accumulation variability on glaciers derived from repeat, spatially extensive ground-penetrating radar surveys,” Cryosphere, vol. 12, no. 11, pp. 3617–3633, Nov. 2018.

[24] R. W. Webb, “Using ground penetrating radar to assess the variability of snow water equivalent and melt in a mixed canopy forest, northern Colorado,” Frontiers Earth Sci., vol. 11, no. 3, pp. 482–495, Sep. 2017.

[25] R. W. Webb, K. S. Jennings, M. Fend, and N. P. Molotch, “Combining ground-penetrating radar with terrestrial LiDAR scanning to estimate the spatial distribution of liquid water content in seasonal snowpacks,” Water Resour. Res., vol. 54, pp. 1–11, Dec. 2018.

[26] N. Griessinger, F. Mohr, and T. Jonas, “Measuring snow ablation rates in Alpine terrain with a mobile multioffset ground-penetrating radar system,” Hydrol. Processes, vol. 32, no. 21, pp. 3272–3282, Sep. 2018.

[27] C. Mitterer, A. Heilig, J. Schweizer, and O. Eisen, “Upward-looking ground-penetrating radar for measuring wet-snow properties,” Cold Regions Sci. Technol., vol. 69, pp. 129–138, Dec. 2011.

[28] R. Kwok et al., “Airborne surveys of snow depth over Arctic sea ice,” J. Geophys. Res., vol. 116, no. C11, pp. 1–16, Nov. 2011.

[29] J. Zhu, S. Tan, J. King, C. Derksen, J. Lemmetyinen, and L. Tsang, “Forward and inverse radar modeling of terrestrial snow using SnowSAR data,” IEEE Trans. Geosci. Remote Sens., vol. 56, no. 12,

pp. 7122–7132, Dec. 2018.

[30] H.-P. Marshall, M. Schneebeli, and G. Koh, “Snow stratigraphy measurements with high-frequency FMCW radar: Comparison with snow micro-penetrometer,” Cold Regions Sci. Technol., vol. 47, nos. 1–2, pp. 108–117, 2007.

[31] J.-B. Yan et al., “Ultrawideband FMCW radar for airborne measurements of snow over sea ice and land,” IEEE Trans. Geosci. Remote Sens., vol. 55, no. 2, pp. 834–843, Feb. 2017.

[32] M. Nolan, C. Larsen, and M. Sturm, “Mapping snow depth from manned aircraft on landscape scales at centimeter resolution using structure-from-motion photogrammetry,” Cryosphere, vol. 9, pp. 1445–1463, Aug. 2015.

[33] J. Goetz and A. Brenning, “Quantifying uncertainties in snow depth mapping from structure from motion photogrammetry in an Alpine area,” Water Resour. Res., vol. 55, no. 9, pp. 7772–7783, Sep. 2019.

[34] P. D. Broxton and W. J. D. van Leeuwen, “Structure from motion of multi-angle RPAS imagery complements larger-scale airborne LiDAR data for cost-effective snow monitoring in mountain forests,” Remote Sens., vol. 12, no. 14, p. 2311, Jul. 2020.

[35] E-Research. (2019). USRP E312 Data Sheet. [Online]. Avail-able: https://www.ettus.com/wp-content/uploads/2019/01/USRP_E312_ Datasheet.pdf

[36] S. Prager, T. Thrivikraman, M. Haynes, J. Stang, D. Hawkins, and M. Moghaddam, “Ultra-wideband synthesis for high-range-resolution software defined radar,” IEEE Trans. Instrum. Meas., vol. 69, no. 6, pp. 3789–3803, Aug. 2019.

[37] AT Lab. (Feb. 2017). Antennas by RFSPACE. [Online]. Available: https://antennatestlab.com/antenna-examples/example-3-vivaldi-antennas-rfspace

[38] (2021). DJI M600 Pro Specs. [Online]. Available: https://www.dji. com/matrice600-pro/info#specs

[39] S. Prager, D. Hawkins, and M. Moghaddam, “Arbitrary nonlinear FM waveform construction and ultra-wideband synthesis,” in Proc. IEEE Int. Geosci. Remote Sens. Symp. (IGARSS), Waikoloa, HI, USA, Oct. 2020, pp. 7037–7040.

[40] S. Prager, T. Thrivikraman, M. Haynes, J. Stang, D. Hawkins, and M. Moghaddam, “Ultra-wideband synthesis for high-range resolution software defined radar,” in Proc. IEEE Radar Conf., Oklahoma City, OK, USA, Apr. 2018, pp. 1089–1094.

[41] D. J. Rabideau, “Nonlinear synthetic wideband waveforms,” in Proc. IEEE Radar Conf., Long Beach, CA, USA, Apr. 2002, pp. 212–219.

[42] B. M. Keel, J. A. Saffold, M. R. Walbridge, and J. Chadwick, “Nonlinear stepped chirp waveforms with subpulse processing for range side lobe suppression,” Proc. SPIE, Radar Sensor Technol. III, Aug. 1998, doi: 10.1117/12.319437.

[43] D. E. Maron, “Frequency-jumped burst waveforms with stretch processing,” in Proc. IEEE Int. Conf. Radar, May 1990, pp. 274–279.

[44] E. Fowle, “The design of FM pulse compression signals,” IEEE Trans. Inf. Theory, vol. IT-10, no.

1, pp. 61–67, Jan. 1964.

[45] S. Boukeffa, Y. Jiang, and T. Jiang, “Sidelobe reduction with nonlinear frequency modulated waveforms,” in Proc. IEEE 7th Int. Colloq. Signal Process. Appl. (CSPA), Mar. 2011, pp. 399–403.

[46] Google Maps. (2021). Satellite Image of Cameron Pass, Colorado.[Online]. Available: https://www.maps.google.com

[47] Sensors and Software. (2021). PulseEKKO GPR. [Online]. Avail-able: https://www.sensoft.ca/wp-content/uploads/2020/08/pulseEKKO-Brochure-and-Ultra-Receiver.pdf

[48] E. J. Ferraro and C. T. Swift, “Comparison of retracking algorithms using airborne radar and laser altimeter measurements of the Greenland ice sheet,” IEEE Trans. Geosci. Remote Sens., vol. 33, no. 3, pp. 700–707, May 1995.

[49] S. Hendricks, L. Stenseng, V. Helm, and C. Haas, “Effects of surface roughness on sea ice freeboard retrieval with an airborne Ku-band SAR radar altimeter,” in Proc. IEEE Int. Geosci. Remote Sens. Symp., Honolulu, HI, USA, Jul. 2010, pp. 3126–3129.

[50] D. Hutchison et al., “Detecting faint curved edges in noisy images,” in Computer Vision, vol. 6314, K. Daniilidis, P. Maragos, and J. Paragios, Eds. Berlin, Germany: Springer, 2010, pp. 750–763.

[51] N. Ofir, M. Galun, S. Alpert, A. Brandt, B. Nadler, and R. Basri, “On detection of faint edges in noisy images,” 2017, arXiv:1706.07717.[Online]. Available: http://arxiv.org/abs/1706.07717

[52] S. Xie and Z. Tu, “Holistically-nested edge detection,” 2015, arXiv:1504.06375. [Online].

Available: http://arxiv.org/abs/1504.06375

[53] F. Ulaby, R. Moore, and A. Fung, Microwave Remote Sensing: Active and Passive, vol. 3. Norwood, MA, USA: Artech House, 1986.

[54] L. Jiao, L. Huo, C. Hu, and P. Tang, “Refined UNet: UNet-based refinement network for cloud and shadow precise segmentation,” Remote Sens., vol. 12, no. 12, p. 2001, Jun. 2020.

[55] Z. Chu, T. Tian, R. Feng, and L. Wang, “Sea-land segmentation with res-UNet and fully connected CRF,” in Proc. IEEE Int. Geosci. Remote Sens. Symp. (IGARSS), Jul. 2019, pp. 3840–3843.

[56] F. Mazeh et al., “Numerical analysis of radar response to snow using multiple backscattering measurements for snow depth retrieval,” Prog. Electromagn. Res. B, vol. 81, pp. 63–80, 2018.

[57] C. Grima et al., “Surface and basal boundary conditions at the southern McMurdo and Ross ice shelves, Antarctica,” J. Glaciol., vol. 65, no. 252, pp. 675–688, Aug. 2019.

[58] P. Hoekstra and D. Spanogle, “Backscatter from snow and ice surfaces at near incident angles,” IEEE Trans. Antennas Propag., vol. AP-20, no. 6, pp. 788–790, Nov. 1972.

[59] CAI Center. (2021). Avalanche Accident Statistics. [Online]. Available: https://www.avalanche.state.co.us/accidents/statistics-and-reporting/

[60] L. L. Scharf, Statistical Signal Processing: Detection, Estimation, and Time Series Analysis. Reading, MA, USA: Addison Wesley, 1991.